Doctoral Dissertation (Censored)

博士論文（要約）

Ionization and dissociation dynamics of H_2O in ultrashort intense near-IR laser fields by the time-dependent adiabatic state method and the time-dependent configuration interaction method

(時間依存断熱状態法と時間依存配置間相互作用法による H_2O の超短高強度近赤外レーザー場におけるイオン化と解離の ダイナミクス)

A Dissertation Submitted for the Degree of Doctor of Philosophy

December 2019

令和元年 12 月博士（理学）申請

Department of Chemistry, Graduate School of Science,

The University of Tokyo

東京大学大学院理学系研究科

化学専攻

Sho Koh

高　翔

Table of Contents

Abstract

When molecules are exposed to an intense laser field, they are strongly coupled with the light field and their structural deformation and bond breaking processes are governed by the light-dressed potential energy surfaces. This thesis consists of two theoretical studies to investigate molecules in intense fields.

In the first study, I performed theoretical calculations and established the assignment of the observed peak profiles to interpret the experimental findings. It was reported that the momentum distribution of protons ejected from H_2O in an ultrashort intense laser field exhibited multiple peak profiles and that these profiles vary sensitively to the laser pulse in the previous experiment. I first performed *ab initio* molecular dynamics calculations using the time-dependent adiabatic state approach to examine the effect of the laser field on the momentum distribution of protons ejected from H_2O^{2+} and showed that the peak positions of the momentum distribution of H^+ ejected through the two-body dissociation of H_2O^{2+} are in good agreement with the experimental data. I also performed time-dependent configuration interaction calculations to estimate the ionization probability of H_2O^{2+} and revealed that the enhanced ionization of H_2O^{2+} plays an import role in the formation of H_2O^{3+}.

In the second study, I extended the heuristic model in which the ionization process is treated by using complex energies in time-dependent configuration interaction single method, so that it can be implemented in the general class of time-dependent configuration interaction methods. I demonstrated the heuristic model and the extended heuristic model to calculate the resonance enhanced ionization rates of H_2^+ and H_2. The results reproduced the ionization rates as a function of internuclear distance in the previous calculations using grid-based and full-dimensional time-dependent Schrödinger equation.

Chapter 1.

General introduction

1.1 Molecules in intense laser field

When molecules are exposed to intense laser fields, a lot of characteristic phenomena can be induced by the strong light-matter interaction [1], such as molecular alignment [2], structure deformation [3]–[6]. Especially, in carbon hydrogen molecules, ultrafast hydrogen migration and H_3^+ formation have been reported [7]–[11].

Since molecules are strongly perturbed by the light field, their structure deformation process and chemical bond breaking process are governed by their light dressed potential energy surface [12],[13]. In these decades, control of chemical bond breaking processes in polyatomic molecules in an intense laser field has been an attractive research topic [14].

1.2 Strong-field processes

In intense laser fields, the non-perturbative ionization processes of atoms can be driven by the strong field. The strong field can induce the distortion of the Coulomb potential and lowering the barrier for ionization. Thus, many non-perturbative characteristic ionization processes can occur in intense fields, such as multi-photon ionization (MPI), above-threshold ionization (ATI) [15],[16], tunnel ionization (TI) [17], and over-the-barrier ionization (OBI).
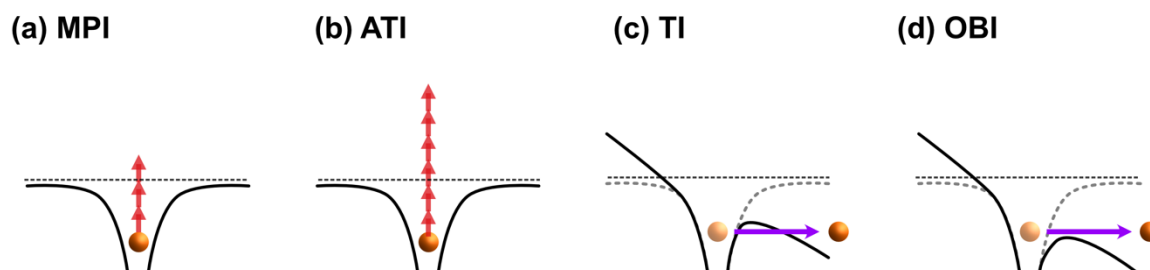
Fig. 1.1. Schematics of ionization processes in intense laser fields. (a) multi-photon ionization (MPI), (b) above-threshold ionization (ATI), (c) tunnel ionization (TI), (d) over-the-barrier ionization (OBI).

As a subsequent process of TI, the photoelectron can be accelerated by the electric field and collides to the parent ion [18]. This electron recollision process can induce many phenomena in intense laser fields, such as rescattering, high-order harmonic generation (HHG) [19],[20], recollisional excitation and non-sequential double ionization (NSDI) [21].

In addition, the expansion of OBI of atoms to molecular system gives a new concept [22], charge resonance enhanced ionization (CREI) [23], in which the ionization rate has peak structures at some internuclear distances.

1.2.1   Above threshold ionization

Above threshold ionization (ATI) is an extension of multi-photon ionization (MPI) in which the number of absorbed photons exceeds the minimum number over ionization threshold I_p [15],[16],[24]. The first observation of ATI photoelectron spectrum is in 1979 [15]. The observed photoelectron spectrum in 532 nm laser field (photon energy is $\hbar\omega = 2.34$ eV) of Xe whose ionization threshold is $I_p = 12.13$ eV is shown in Fig. 1.2. The photoelectron spectrum E_{photon} for ATI is given by

$$E_{photon} = (n + s)\hbar\omega - I_p, \tag{1.1}$$

where n represents the minimal number of photons to exceed ionization threshold I_p, and the s represents the number of additional photons absorbed. In Fig. 1.2, the photoelectron spectrum (cycles) exhibits two peaks. The peak located at $E_{photon} \simeq 2$ eV is corresponding to $n = 6$, which is the minimum number of photons to exceed the ionization threshold. The peak appearing at $E_{photon} \simeq 4.5$ eV is corresponding to $s = 1$, that is, one extra photon absorption for ionization, showing the occurrence of ATI process.
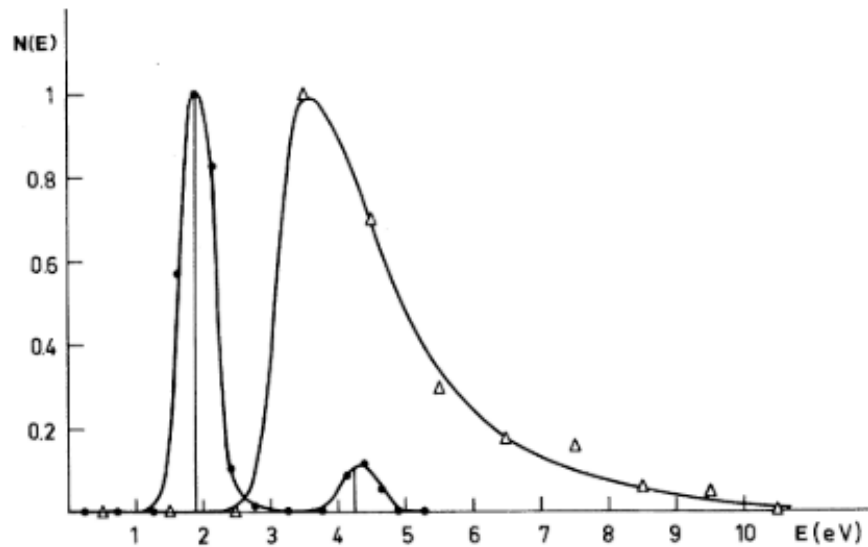
Fig. 1.2. Energy spectra of the emitted electrons for two photon energies from Xe: triangles, $\hbar\omega = 1.17$ eV, $I = 4 \times 10^{13}$ W/cm^{-2}; circles, $\hbar\omega = 2.34$ eV, $I = 8 \times 10^{12}$ W/cm^{-2}, adopted from [15].

1.2.2 Tunneling ionization

Tunneling ionization is a process in which the electrons escape from the atoms or molecules through the distorted potential barrier within a half cycle of the electric field as shown in Fig. 1.3. S. L. Chin observed the existence of tunnel ionization of Xe atoms using a CO$_2$ laser in 1985 [25]. Tunneling ionization is a quantum mechanical phenomenon, which cannot be described using a classical picture because an electron does not have enough energy to pass through the potential barrier.
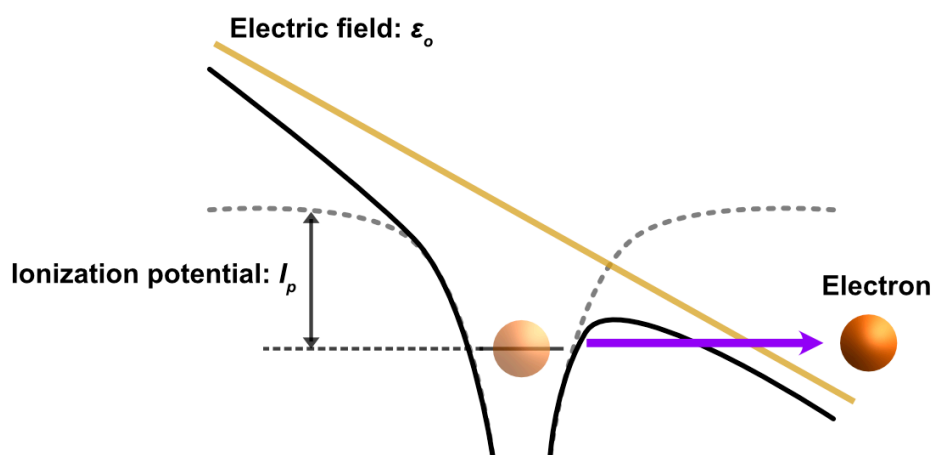
Fig. 1.3. Schematic picture of tunneling ionization process.

Ammosov, Delone and Krainov [26] developed a model to calculate the tunneling ionization rates for atoms in a quasi-static field, known as ADK model. In ADK model, the tunnel ionization rate of a hydrogen atom-like atom in a static electric field ε_o in atomic units is given by

$$W^{ADK} = |C_{n^*l^*}|^2 f_{lm} I_p \left(\frac{2\kappa^3}{\varepsilon_o}\right)^{2n^*-|m|-1} \exp\left(-\frac{2\kappa^3}{3\varepsilon_o}\right), \tag{1.2}$$

where I_p is the ionization potential of the atom, the factor κ is given by

$$\kappa = \sqrt{2I_p}. \tag{1.3}$$

$C_{n^*l^*}$ and f_{lm} contain the information about the initial atomic state. $C_{n^*l^*}$ is given by

$$|C_{n^*l^*}|^2 = \frac{2^{2n^*}}{n^*\Gamma(n^* + l^* + 1)\Gamma(n^* - l^*)}, \tag{1.4}$$

where $n^* = Z/\sqrt{I_P}$, Z being the charge of the atomic core, and $l^* = n^* - 1$, Γ denotes the Gamma function. The factor f_{lm} is

$$f_{lm} = \frac{(2l + 1)}{2^{|m|}|m|!} \frac{(l + |m|)!}{(l - |m|)!}, \tag{1.5}$$

with l, m denoting electrons initial orbital and magnetic quantum numbers.

As the extension to molecular systems, Tong *et al.* [27],[28] introduced a molecular ADK model (MO-ADK). MO-ADK is based on the assumptions of the ADK model which is derived for an electronic state with a well-defined spherical harmonic. In MO-ADK model, the molecular wavefunction is expressed as the linear combination of atomic spherical harmonics in the asymptotic region as

$$\Psi^m(\boldsymbol{r}) = \sum_l C_{lm} F_{lm}(r) Y_{lm}(\hat{\boldsymbol{r}}), \tag{1.6}$$

where m is the magnetic quantum along the molecular axis, C_{lm} is the coefficient which is normalized in such a way that the radial wavefunction in the asymptotic region can be written as

$$F_{lm}(r \to \infty) \approx r^{\frac{Z}{\kappa}-1} \exp(-\kappa r), \tag{1.7}$$

where Z denotes the effective charge. On the assumption that the molecular axis is along the external field direction, the electron will be ionized along the field direction $\theta \simeq 0$. The leading term of the spherical harmonic along this direction $Y_{lm}(\hat{\boldsymbol{r}})$ is given by

$$Y_{lm}(\hat{r}) \simeq Q(l,m) \frac{\sin^{|m|}(\theta)}{2^{|m|}|m|!} \frac{e^{im\varphi}}{\sqrt{2\pi}}, \tag{1.8}$$

with

$$Q(l,m) = (-1)^m \sqrt{\frac{(2l+1)(1+|m|)!}{2(l-|m|)!}}. \tag{1.9}$$

By substituting Eq. (1.7) and (1.8) into Eq. (1.6), the wave function in the tunneling region can be written as

$$\Psi^m(\boldsymbol{r}) \simeq \sum_l C_{lm} r^{\frac{z}{\kappa}-1} \exp(-\kappa r) Q(l,m) \frac{\sin^{|m|}(\theta)}{2^{|m|}|m|!} \frac{e^{im\varphi}}{\sqrt{2\pi}}$$
$$\simeq \sum_l B(m) r^{\frac{z}{\kappa}-1} \exp(-\kappa r) \frac{\sin^{|m|}(\theta)}{2^{|m|}|m|!} \frac{e^{im\varphi}}{\sqrt{2\pi}}, \tag{1.10}$$

with

$$B(m) = \sum_l C_{lm} Q(l,m). \tag{1.11}$$

The ionization rate for a diatomic molecule with its axis aligned with the static field strength ε_o is given by

$$W^{MO-ADK}(\varepsilon_o, 0) = \frac{B^2(m)}{2^{|m|}|m|!} \frac{1}{\kappa^{\frac{2Z}{\kappa}-1}} \left(\frac{2\kappa^3}{\varepsilon_o}\right)^{\frac{2Z}{\kappa}-|m|-1} \exp\left(-\frac{2\kappa^3}{3\varepsilon_o}\right). \tag{1.12}$$

Considering the rotation of the field direction from the molecular axis, the MO-ADK ionization rate can be given by

$$W^{MO-ADK}(\varepsilon_o, \boldsymbol{\Omega}) = \sum_{m'} \frac{B^2(m')}{2^{|m'|}|m'|!} \frac{1}{\kappa^{\frac{2Z}{\kappa}-1}} \left(\frac{2\kappa^3}{\varepsilon_o}\right)^{\frac{2Z}{\kappa}-|m'|-1} \exp\left(-\frac{2\kappa^3}{3\varepsilon_o}\right), \tag{1.13}$$

where

$$B(m') = \sum_l C_{lm} Q(l,m') D^l_{m',m}(\boldsymbol{\Omega}), \tag{1.14}$$

$D^l_{m',m}(\boldsymbol{\Omega})$ denotes the rotation matrix and $\boldsymbol{\Omega}$ denotes the Euler angles between the molecular axis and the field direction.

1.2.3　Over-the-barrier ionization

If the laser field strength is further increased, then the barrier becomes below the ionization potential and the electron escapes directly over the barrier without tunneling [29]–[32] as shown in Fig. 1.1 (d). This phenomenon is called as over-the-barrier ionization (OBI).

1.2.4　Keldysh parameter

It is known that the three ionization regimes of ATI, TI and OBI can be distinguish by the Keldysh parameter [17], given by

$$\gamma = \sqrt{\frac{I_p}{2U_p}},$$

(1.15)

where I_p is the ionization potential and U_p is the ponderomotive energy, which is the average kinetic energy of a free electron in a linearly polarized field $\varepsilon_o \cos \omega t$, given by

$$U_p = \frac{e^2 \varepsilon_o^2}{4 m_e \omega^2} = \frac{e^2}{8\pi^2 m_e \epsilon_o c^3} I_o^2 \lambda^2,$$

(1.16)

where e is the charge of electron, ε_o is the electric field strength, m_e is the mass of an electron, ω is the central laser frequency, λ is wavelength, I_o is intensity, ϵ_o is the vacuum permittivity, and c is the speed of light. The Keldysh parameter can be interpreted as a value of the time for the electron to pass through the barrier (tunneling time) divides by half of the laser cycle, as

$$\gamma = \frac{\text{tunneling time}}{\text{half of the laser cycle}}.$$

(1.17)

When $\gamma > 1$, since the oscillation period of the electric field is much shorter than tunneling time, MPI becomes the dominant ionization process. One the other hand, when $\gamma < 1$, TI and OBI dominate over MPI because the electron has enough time to pass through the distorted barrier by the electric field.

1.2.5　Electron recollision process

When atoms or molecules are ionized by a linear or slightly elliptical laser light, the electric field can drive an ionized electron to return to the parent ion with a significant kinetic energy.

A semi-classical picture, called as simple man's model [18],[33], gives an intuitive understanding of electron recollison process. The simple man's model is also known as the three-step or recollision model. In this model, the recollision process is decomposed into the

following three steps: (1) generation of a free electron through tunneling ionization process, (2) electron acceleration by laser field, (3) electron collision, as illustrated in Fig. 1.4.
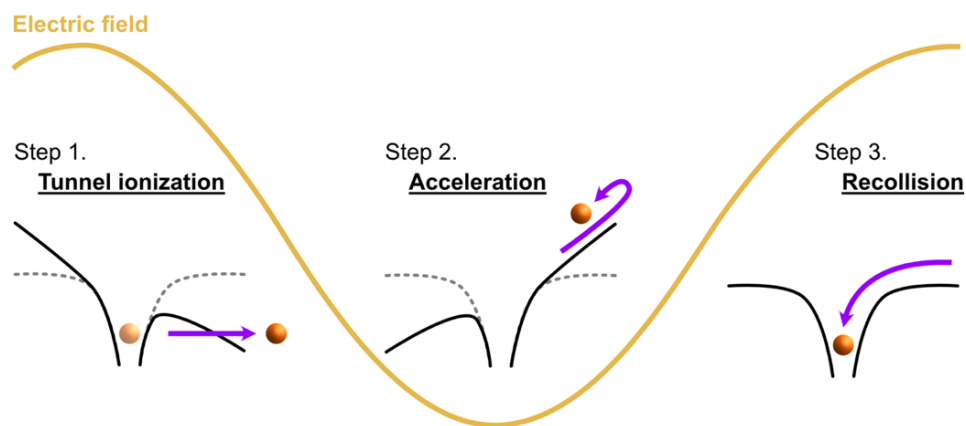
Fig. 1.4. Schematic of the electron recollision process in one cycle of the electric field.

In the first ionization step, the potential gets strongly distorted in the presence of the relatively slowly varying strong electric field and the ionized electron will be born at the atomic of molecular core with zero velocity. In the second electron acceleration step, the motion of the ejected electron can be obtained by solving Newton's equation of motion in a laser electric field $\boldsymbol{\varepsilon}(t)$ as

$$\frac{d\boldsymbol{p}_{elec}(t)}{dt} = -e\boldsymbol{\varepsilon}(t), \tag{1.18}$$

where $\boldsymbol{p}_{elec}(t)$ is the momentum of the ejected electron as a function of time t, e denotes the charge of electron.

The subsequent recollision can induce various physical processes such as electron rescattering, high-order harmonic generation (HHG), recollisional excitation, non-sequential double or non-sequential multiple ionization (NSDI).
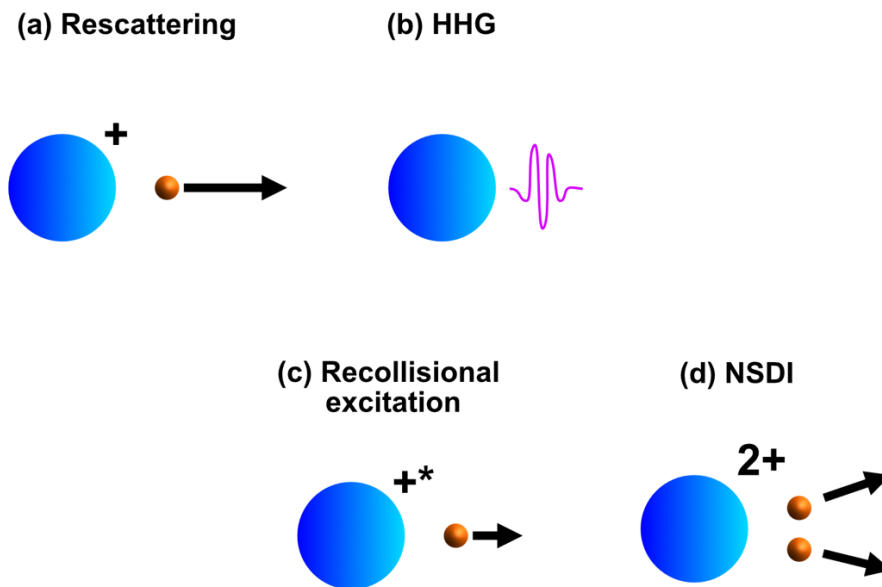
Fig. 1.5. Schematics of the subsequent phenomena of electron recollision: (a) Rescatterting (b) High-order harmonic generation (HHG) (c) Recollisional excitation (d) Non-sequential double ionization (NSDI)

1.2.5.1 High-order harmonic generation

The high-order harmonics of the the fundamental laser light can be generated through the electron recombination, known as high-order harmonic generation (HHG). HHG can produce high photon energies in the extreme ultraviolet and x-ray energy region. The first observations of HHG were in 1988 [19],[20]. The HH spectrum has a characteristic shape as shown in Fig. 1.6, in which a plateau structure can be seen. According to simple man's model, the end of the plateau structure, namely the cut-off energy, can be calculated as [8]

$$E_{cutoff} = I_p + 3.17U_p,$$ (1.19)

where I_p is the ionization potential and U_p is the ponderomotive energy.
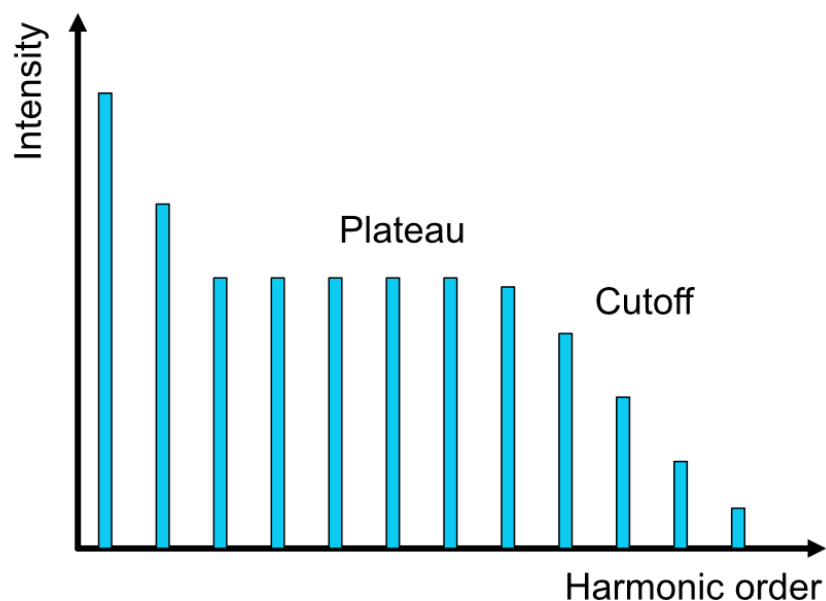
Fig. 1.6. Typical shape of the high harmonic spectrum.

1.2.5.2   Non-sequential double ionization

The returning electron to the parent ion can induce the ejection of another electron if it has enough energy. This process is known as non-sequential double ionization (NSDI) [34]. NSDI can proceed through two ionization pathways after the first electron recollision [21],[35] The first pathway is the direct ionization of the second electron induced by the impact of the first returning electron [18]. The second one is the ionization in which excitation is induced by impact and the subsequent tunnel ionization occurs with a delay, known as recollision-excitation with subsequent ionization (RESI) [36].

1.2.6   Enhanced ionization

In a molecular system, as increasing of the internuclear distance R of molecular systems induced by strong laser fields, there are some critical distances R_c where ionization rate takes a peak structure. For symmetric molecules, this phenomenon, known as charge resonance enhanced ionization (CREI) [37]–[39], has been investigated in several studies. CREI is an extension of over-the-barrier ionization (OBI) into the molecular system [22].
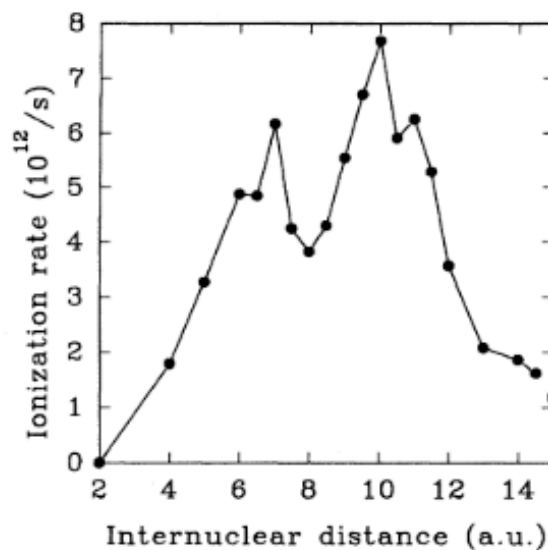
Fig. 1.7. Ionization rate of the H_2^+ molecular ion in 10^{14} W/cm^2, 1064 nm, linearly polarized laser fields (five-cycle linear rise) adopted from [39]. The square on the right vertical axis marks the ionization of the hydrogen atom.

For the simplest system H_2^+, Zuo *et al.* [39] calculated the ionization rates as a function of internuclear distance R for a 10^{14} W/cm^2, 1064 nm, linearly polarized laser field as shown in Fig. 1.7. The enhancement of ionization rates can be seen in the range of $5 < R < 12$ a.u.. The mechanism can be explained as the effect of the formation of charge resonance states in a static field picture. In an electric static field, the upper level σ_+ lies just above the inner barrier and it can ionize directly over the barrier at $R = 10$ a.u. as shown in Fig. 1.8. Furthermore, the coupling of the charge resonance states to the external field at large R guarantees that the population of the upper level σ_+ is substantial. Therefore, the peak structure of ionization rates can be seen there.
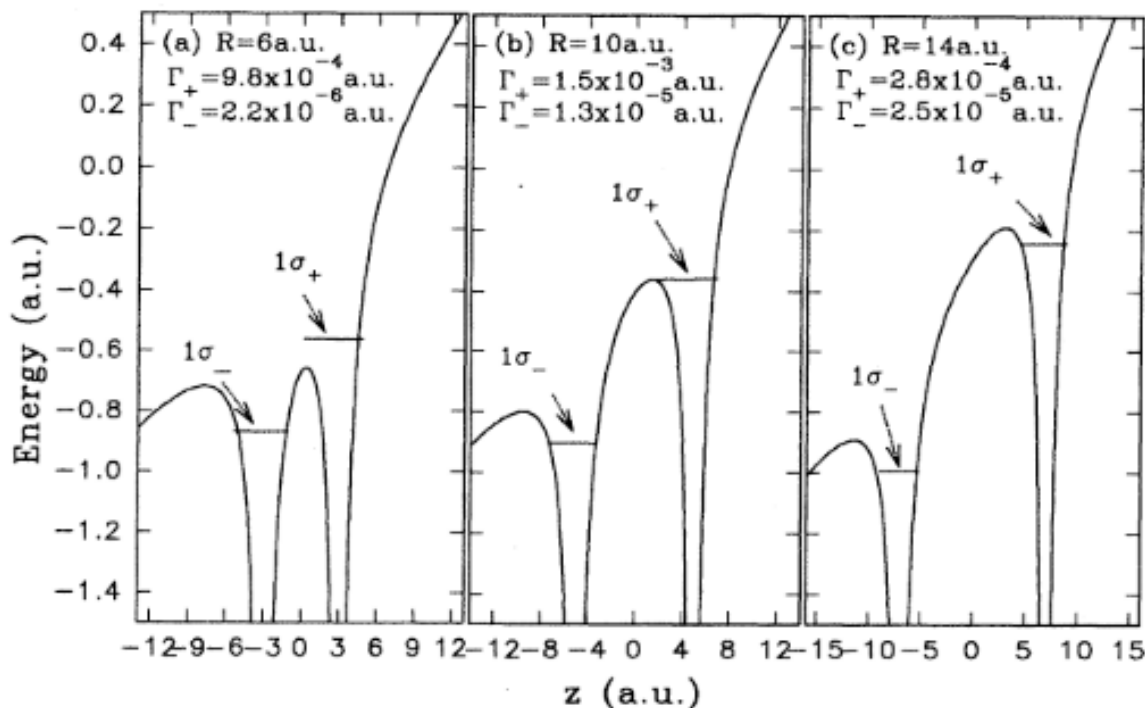
Fig. 1.8. Lowest two dc-field-induced levels of H_2^+, σ_+ and σ_-, in the effective potential where the field intensity is 10^{14} W/cm^2 [39]. Γ_+ and Γ_- denote the ionization rates of the level σ_+ and σ_-, respectively.

1.3 Present studies

In this thesis study, I theoretically investigated the interaction between molecules and strong light fields.

In Chapter 1, several typical phenomena of atoms and molecules in intense fields are introduced.

In Chapter 2, I show that the theoretical background for treating the electronic dynamics and molecular dynamics in intense laser fields. The methods for simulating the dynamics of electrons and molecules, such as *ab initio* molecular dynamics, time-dependent adiabatic state approach and time-dependent configuration interaction, are introduced.

In Chapter 3, I show my theoretical calculation about water (H_2O) molecule in ultrashort intense laser fields to interpret the previous experiment. I performed *ab initio* molecular dynamics calculation combined with time-dependent adiabatic state approach to simulate the dissociation dynamics of H_2O^{2+}. I also demonstrated time-dependent configuration interaction calculation to investigate ionization process of H_2O^{2+}.

In Chapter 4, the heuristic model proposed by Klinkusch *et al.* [40], in which the ionization process is treated by using complex energies in time-dependent configuration

interaction single method, was extended to be implementable in the general class of time-dependent configuration interaction methods. I demonstrated the heuristic model and the extended heuristic model to calculate charge resonance enhanced ionization rate of H_2^+ and H_2.

In Chapter 5, I show the summary of this thesis and the future perspectives.

References

[1] K. Yamanouchi, *Science.* **295**, 1659 (2002).

[2] H. Stapelfeldt and T. Seideman, *Rev. Mod. Phys.* **75**, 543 (2003).

[3] A. Hishikawa, A. Iwamae, and K. Yamanouchi, *J. Chem. Phys.* **111**, 8871 (1999).

[4] A. Hishikawa, A. Iwamae, and K. Yamanouchi, *Phys. Rev. Lett.* **83**, 1127 (1999).

[5] H. Hasegawa, A. Hishikawa, and K. Yamanouchi, *Chem. Phys. Lett.* **349**, 57 (2001).

[6] A. Iwasaki, A. Hishikawa, and K. Yamanouchi, *Chem. Phys. Lett.* **346**, 379 (2001).

[7] Y. Furukawa, K. Hoshina, K. Yamanouchi, and H. Nakano, *Chem. Phys. Lett.* **414**, 117 (2005).

[8] T. Okino, Y. Furukawa, P. Liu, T. Ichikawa, R. Itakura, K. Hoshina, K. Yamanouchi, and H. Nakano, *Chem. Phys. Lett.* **419**, 223 (2006).

[9] T. Okino, Y. Furukawa, P. Liu, T. Ichikawa, R. Itakura, K. Hoshina, K. Yamanouchi, and H. Nakano, *Chem. Phys. Lett.* **423**, 220 (2006).

[10] K. Hoshina, Y. Furukawa, T. Okino, and K. Yamanouchi, *J. Chem. Phys.* **129**, 104302 (2008).

[11] D. Mathur, A.K. Dharmadhikari, J.A. Dharmadhikari, and P. Vasa, *J. Phys. B At. Mol. Opt. Phys.* **50**, 154004 (2017).

[12] H. Kono, S. Koseki, M. Shiota, and Y. Fujimura, *J. Phys. Chem. A* **105**, 5627 (2001).

[13] H. Kono, Y. Sato, N. Tanaka, T. Kato, K. Nakai, S. Koseki, and Y. Fujimura, *Chem. Phys.* **304**, 203 (2004).

[14] R. Itakura, K. Yamanouchi, T. Tanabe, T. Okamoto, and F. Kannari, *J. Chem. Phys.* **119**, 4179 (2003).

[15] P. Agostini, F. Fabre, G. Mainfray, G. Petite, and N.K. Rahman, *Phys. Rev. Lett.* **42**, 1127 (1979).

[16] M. Protopapas, C.H. Keitel, and P.L. Knight, *Reports Prog. Phys.* **60**, 389 (1997).

[17] L. V. Keldysh, *Sov. Phys. JETP* **20**, 1307 (1965).

[18] P.B. Corkum, *Phys. Rev. Lett.* **71**, 1994 (1993).

[19] M. Ferray, A. L'Huillier, X.F. Li, L.A. Lompre, G. Mainfray, and C. Manus, *J. Phys. B At. Mol. Opt. Phys.* **21**, (1988).

[20] A. McPherson, G. Gibson, H. Jara, U. Johann, T.S. Luk, I.A. McIntyre, K. Boyer, and C.K. Rhodes, *J. Opt. Soc. Am. B* **4**, 595 (1987).

[21] D.N. Fittinghoff, P.R. Bolton, B. Chang, and K.C. Kulander, *Phys. Rev. Lett.* **69**, 2642

(1992).

[22] A. Bandrauk and F. Légaré, *Progress in Ultrafast Intense Laser Science VIII* (Springer Berlin Heidelberg, Berlin, Heidelberg, 2012).

[23] K. Codling and L.J. Frasinski, *J. Phys. B At. Mol. Opt. Phys.* **26**, 783 (1993).

[24] F. Fabre, G. Petite, P. Agostini, and M. Clement, *J. Phys. B At. Mol. Phys.* **15**, 1353 (1982).

[25] S.L. Chin, F. Yergeau, and P. Lavigne, *J. Phys. B At. Mol. Phys.* **18**, 14 (1985).

[26] M. V. Ammosov, N.B. Delone, and V.P. Krainov, *Sov. Phys. JETP* **64**, 1191 (1986).

[27] X.M. Tong, Z.X. Zhao, and C.D. Lin, *Phys. Rev. A* **66**, 033402 (2002).

[28] X.M. Tong, Z.X. Zhao, and C.D. Lin, *J. Mod. Opt.* **52**, 185 (2005).

[29] S. Augst, D. Strickland, D.D. Meyerhofer, S.L. Chin, and J.H. Eberly, *Phys. Rev. Lett.* **63**, 2212 (1989).

[30] S. Augst, D.D. Meyerhofer, D. Strickland, and S.L. Chint, *J. Opt. Soc. Am. B* **8**, 858 (1991).

[31] V.P. Krainov, *J. Opt. Soc. Am. B* **14**, 425 (1997).

[32] A. Scrinzi, M. Geissler, and T. Brabec, *Phys. Rev. Lett.* **83**, 706 (1999).

[33] G.G. Paulus, W. Becker, W. Nicklich, and H. Walther, *J. Phys. B At. Mol. Opt. Phys.* **27**, (1994).

[34] B. Walker, B. Sheehy, L.F. DiMauro, P. Agostini, K.J. Schafer, and K.C. Kulander, *Phys. Rev. Lett.* **73**, 1227 (1994).

[35] M.G. Pullen, B. Wolter, X. Wang, X.M. Tong, M. Sclafani, M. Baudisch, H. Pires, C.D. Schröter, J. Ullrich, T. Pfeifer, R. Moshammer, J.H. Eberly, and J. Biegert, *Phys. Rev. A* **96**, 1 (2017).

[36] B. Feuerstein, R. Moshammer, D. Fischer, A. Dorn, C.D. Schröter, J. Deipenwisch, J.R. Crespo Lopez-Urrutia, C. Höhr, P. Neumayer, J. Ullrich, H. Rottke, C. Trump, M. Wittmann, G. Korn, and W. Sandner, *Phys. Rev. Lett.* **87**, 43003 (2001).

[37] K. Codling, L.J. Frasinski, and P.A. Hatherly, *J. Phys. B At. Mol. Opt. Phys.* **22**, L321 (1989).

[38] T. Seideman, M.Y. Ivanov, and P.B. Corkum, *Phys. Rev. Lett.* **75**, 2819 (1995).

[39] T. Zuo and A.D. Bandrauk, *Phys. Rev. A* **52**, R2511 (1995).

[40] S. Klinkusch, P. Saalfrank, and T. Klamroth, *J. Chem. Phys.* **131**, 114304 (2009).

Chapter 2.

Theoretical background

2.1 *Ab initio* molecular dynamics

2.1.1 Introduction

Molecular dynamics is a well-established method for numerically solving Newton's equations of motion to simulate the physical movement of atoms and molecules. To describe the dynamics accurately, it is essential to know the internuclear forces obtained from first principles by using a quantum mechanical method.

Based on Born-Oppenheimer approximation [1], the nuclear motions can be described as the classical trajectories on the potential energy surface calculated using *ab initio* electronic state calculation. This approach is called *ab initio* molecular dynamics [2]–[7]. Because the electronic structure is treated explicitly in *ab initio* molecular dynamics, the forces acting on the nuclei, the dipole moment and other molecular properties can be calculated with the accuracy determined by the electronic structure representation. As another advantage of *ab initio* molecular dynamics, the whole potential energy surface is not necessary because the molecular geometry and the velocities of nuclei are only determined by the information at the previous time step. Therefore, after preparation of the initial coordinates and the initial velocities of nuclei, the time evolution can be proceeded with "on-the-fly" electronic structure calculations.

I developed an *ab initio* molecular dynamics program using Haskell programming language for simulating isolated molecular systems in intense laser fields. Haskell is a statically typed and purely functional programming language so that it enables a program with few bugs and easier parallelization. The procedure of molecular dynamics simulation consists of three steps: (1) Preparation of initial conditions, (2) Time integration and (3) Data analysis. At the beginning, I show the theoretical background of *ab initio* molecular dynamics. Next, I show how to generate the sampling as Wigner distribution which is a typical method for generating the initial conditions in high vacuum conditions, and how to prepare the random orientations of molecules. Finally, I show the several techniques to do time integration and data analysis.

2.1.2 Theory

In *ab initio* molecular dynamics, the nuclear motion is described as classical trajectories on the potential energy surface calculated from *ab initio* electronic structure calculation [5],[7]. The concept is based on Born-Oppenheimer approximation [1] in which the electrons and nuclei can be treated separately. The motion of nuclei is much slower than that of electrons because the masses of the nuclei is much heavier than the electron mass. Thus, it is possible to assume the coordinates of nuclei are fixed in the calculation for the electronic motion.

The non-relativistic Hamiltonian for a molecular system which includes n electrons and N nuclei under a field-free condition is given by

$$\hat{H} = -\sum_{I=1}^{N} \frac{\hbar^2}{2M_I} \nabla_I^2 - \sum_{i=1}^{n} \frac{\hbar^2}{2m_e} \nabla_i^2 + \sum_{i>j} \frac{e^2}{|r_i - r_j|} + \sum_{l>J} \frac{Z_l Z_J e^2}{|R_l - R_J|} - \sum_{i,l} \frac{Z_l e^2}{|R_l - r_i|}$$

$$\equiv \hat{T}_n + \hat{T}_e + V_{ee}(r) + V_{nn}(R) + V_{en}(r, R), \tag{2.1}$$

where the electrons are described by coordinates $r_1, r_2, \dots, r_n \equiv r$, mass m_e and charge e, and the nuclei are described by coordinates $R_1, R_2, \dots, R_N \equiv R$, masses $M_1, M_2, \dots, M_N$ and charges $Z_1 e, Z_2 e, \dots, Z_N e$. In the second line, $\hat{T}_n, \hat{T}_e, V_{ee}(r), V_{nn}(R)$ and $V_{en}(r, R)$ denote the nuclear and electron kinetic energy operators and electron-electron, nuclear-nuclear and electron–nuclear interaction potential operators, respectively. The time-independent Schrödinger equation for $\hat{H}$ is given by

$$\hat{H}\Psi(x, R) = E\Psi(x, R), \tag{2.2}$$

where $x \equiv (r, s)$ denotes the coordinates of electron position including spin variables, and $\Psi(x, R)$ is an eigenfunction of $\hat{H}$ with eigenvalue E. This equation cannot be solved easily because the entanglement of the motions of electrons and nuclei. In Born-Oppenheimer approximation, where the electronic motion and nuclear motion are separated because the electrons are lighter than the nuclei by three orders of magnitude, the wavefunction $\Psi(x, R)$ can be expressed as

$$\Psi(x, R) = \phi(x; R)\chi(R), \tag{2.3}$$

where $\chi(R)$ is the nuclear wavefunction and $\phi(x; R)$ is the electronic wavefunction which is parametric dependence on the nuclear positions R. Note only the electronic ground state is considered here. Substitution of Eq. (2.3) into Eq. (2.2) and recognition that R is fixed in $\phi(x; R)$, that is, $\hat{T}_n \phi(x; R) = 0$, yields

$$E\phi(x; R)\chi(R) = \left(\hat{T}_n + \hat{T}_e + V_{ee}(r) + V_{nn}(R) + V_{en}(r, R)\right)\phi(x; R)\chi(R)$$

$$= \chi(R)\left(\hat{T}_e + V_{ee}(r) + V_{nn}(R) + V_{en}(r, R)\right)\phi(x; R) + \phi(x; R)\hat{T}_n\chi(R). \quad (2.4)$$

Note $V_{nn}(R)$ is a constant when R is fixed. Dividing both sides by $\phi(x; R)\chi(R)$, Eq. (2.4) can be transformed as

$$\frac{\hat{T}_e + \hat{V}_{ee}(r) + V_{nn}(R) + V_{en}(r, R)}{\phi(x; R)}\phi(x; R) = E - \frac{\hat{T}_n\chi(R)}{\chi(R)}. \quad (2.5)$$

In this equation, the left-hand side is a function of x and R, and the right-hand side is a function only of R. It must be a function only of R for both sides to be established for all x. Let this function be denoted $g(R)$ and

$$\hat{H}_{el} \equiv \hat{T}_e + V_{ee}(r) + V_{nn}(R) + V_{en}(r, R), \quad (2.6)$$

where $\hat{H}_{el}$ is called as the electronic Hamiltonian. Thus,

$$\hat{H}_{el}\phi(x; R) = g(R)\phi(x; R), \quad (2.7)$$

$$\left(\hat{T}_n + g(R)\right)\chi(R) = E\chi(R). \quad (2.8)$$

Eq. (2.7) shows the eigenvalue equation about the electronic state at a fixed nuclear position and Eq. (2.8) is the nuclear eigenvalue equation. $g(R)$ expresses the potential energy surface on which the nuclear packet moves.

The nuclear dynamics is determined by a time-dependent Schrödinger equation for the time-dependent nuclear wavefunction $X(R, t)$ as

$$i\hbar\frac{\partial}{\partial t}X(R, t) = \left(\hat{T}_n + g(R)\right)X(R, t). \quad (2.9)$$

To extract classical mechanics from quantum mechanics, $X(R, t)$ is rewritten to the corresponding wave function in a polar representation as

$$X(R, t) = A(R, t)\exp\left(\frac{i}{\hbar}S(R, t)\right) \quad (2.10)$$

in terms of an amplitude factor A and a phase S which both are real values. Substituting Eq. (2.10) into Eq. (2.9) and separating the real and imaginary parts, the separated equations for S and A can be obtained as [5],[7].

$$\frac{\partial S}{\partial t} + \sum_I \frac{(\nabla_I S)^2}{2M_I} + g(R) = \hbar^2 \sum_I \frac{1}{2M_I}\frac{\nabla_I^2 A}{A}, \quad (2.11)$$

$$\frac{\partial A}{\partial t} + \sum_I \frac{(\nabla_I A)(\nabla_I S)}{M_I} + \sum_I \frac{A(\nabla_I^2 S)}{2M_I} = 0. \quad (2.12)$$

In the classical limit $\hbar \to 0$, Eq. (2.11) is given by

$$\frac{\partial S}{\partial t} + \sum_I \frac{(\nabla_I S)^2}{2M_I} + g(\boldsymbol{R}) = 0. \tag{2.13}$$

Eq. (2.12), which is independent of $\hbar$, can be rewritten as a continuity equation [7], showing the variation of the nuclear density $|X|^2 = A^2$. By introducing

$$\boldsymbol{P}_I \equiv \nabla_I S, \tag{2.14}$$

Eq. (2.13) can be rewritten as

$$\frac{\partial S}{\partial t} + \sum_I \frac{\boldsymbol{P}_I^2}{2M_I} + g(\boldsymbol{R}) = 0. \tag{2.15}$$

The resulting equation is just the classical Hamiltonian–Jacobi equation with the classical Hamilton function

$$H(\{\boldsymbol{R}_I\}, \{\boldsymbol{P}_I\}) \equiv \sum_I \frac{\boldsymbol{P}_I^2}{2M_I} + g(\boldsymbol{R}), \tag{2.16}$$

which is defined in terms of the nuclear coordinates $\{\boldsymbol{R}_I\}$ and their conjugate momenta $\{\boldsymbol{P}_I\}$. The Hamilton–Jacobi equation is equivalent to Newton equation of motion, given by

$$\frac{d\boldsymbol{P}_I}{dt} = -\nabla_I g(\boldsymbol{R}) \tag{2.17}$$

or

$$M_I \frac{d^2 \boldsymbol{R}_I}{dt^2} = -\nabla_I g(\boldsymbol{R}). \tag{2.18}$$

Therefore, the nuclear dynamics can be described as the classical trajectories on the potential energy surface calculated as the electronic eigenenergy $g(\boldsymbol{R})$ using Eq. (2.7).

2.1.3 Preparation of initial conditions

2.1.3.1 Sampling from Wigner distribution

In order to obtain accurate results from *ab initio* molecular dynamics, it is important to prepare a proper ensemble of trajectories. As shown in Fig. 2.1, for vibrational ground state, the classical distribution is clearly different from the quantum one, in which the peak locates at the equilibrium value. One the other hand, both the quantum and classical distributions become similar for the higher vibrational state. For simulating isolated molecular systems under high vacuum, the Wigner distribution function [8]–[10] may be used to select the initial

coordinates and momentum of each nucleus for each trajectory. Each vibrational mode in a molecule can be assumed as a one-dimensional harmonic oscillator, and the initial coordinates and momentum are sampled from its Wigner distribution. For a molecule which has multiple vibrational modes, the total Wigner distribution function can be expressed as the product of the Wigner function of all vibrational modes.
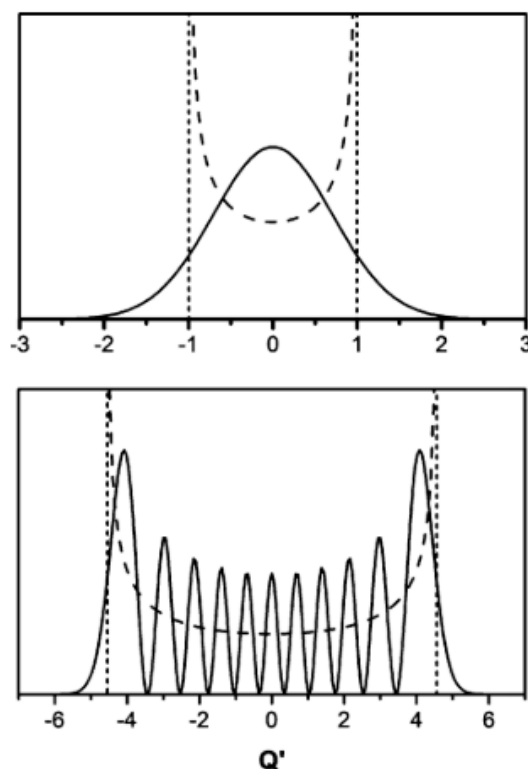
Fig. 2.1. Comparison of quantum (solid) and classical (dashed) probability distributions of the normal mode coordinate Q' for the quantum states $n = 0$ (top) and 10 (bottom) [11].

Wigner distribution function, which is a function of positions q and momentum p, defined as [8]

$$W(q, p) \equiv \frac{1}{(2\pi\hbar)^N} \int d\,s \exp(ip \cdot s/\hbar)\, \Psi(q - s/2)\Psi(q + s/2), \quad (2.19)$$

where s is a spatial variable and N is the number of dimensions.

The Hamiltonian of a harmonic oscillator with mass m and angular frequency ω is

$$\widehat{\mathcal{H}} = \frac{1}{2}m\omega^2\hat{x}^2 + \frac{\hat{p}^2}{2m}, \quad (2.20)$$

where $\hat{x}$ is the position operator and $\hat{p}$ is the momentum operator. The eigenenergy ε_n for nth state is given as

$$\varepsilon_n = \hbar\omega\left(n + \frac{1}{2}\right). \tag{2.21}$$

The dimensionless coordinates $\hat{Q}$ and momentum operators $\hat{P}$ are defined as [12]

$$\hat{Q} = \sqrt{\frac{m\omega}{\hbar}}\,\hat{x}, \tag{2.22}$$

$$\hat{P} = \sqrt{\frac{1}{m\omega\hbar}}\,\hat{p}. \tag{2.23}$$

The Hamiltonian in Eq. (2.20) can be converted as

$$\hat{H} = \frac{1}{2}\hat{P}^2 + \frac{1}{2}\hat{Q}^2, \tag{2.24}$$

and the eigenenergy is

$$E_n = \frac{\varepsilon_n}{\hbar\omega} = n + \frac{1}{2}. \tag{2.25}$$

It is known that the wavefunction for the harmonic oscillator in Eq. (2.24) in nth state is [12]

$$\psi_n(Q) = \left(\pi^{1/2}2^n n!\right)^{-1/2} H_n(Q)\exp\left(-\frac{1}{2}Q^2\right), \tag{2.26}$$

where $H_n(Q)$ is the nth Hermite polynomial. Inserting this equation into Eq. (2.19), the Wigner distribution for the wavefunction of a harmonic oscillator can be given as [12]

$$W^{(n)}(Q, P) = (-1)^n (\pi n!) L_n(\rho) e^{-\rho^2/2}, \tag{2.27}$$

where $L_n(\rho)$ is the nth order Laguerre polynomial and ρ is given by

$$\rho^2 = 2(P^2 + Q^2). \tag{2.28}$$

For the vibrational ground state, $n = 0$, $W^{(n=0)}(Q, P)$ can be written in a simple form as the product of two Gaussian functions

$$W^{(n=0)}(Q, P) = \frac{1}{\pi\hbar}e^{-Q^2}e^{-P^2}. \tag{2.29}$$

In the case of a molecule with N vibrational modes, by assuming each mode is independent, the Wigner distribution $W(\boldsymbol{Q}, \boldsymbol{P})$ for all vibrational modes can be written as a product of the Wigner distributions of all vibrational modes, as

$$W(Q, P) = \prod_{i=1}^{N} W(Q_i, P_i). \tag{2.30}$$

For vibrational mode i, in order to generate (Q_i, P_i) as a Wigner distribution in Eq. (2.29), Neumann's rejection method [13] can be used. Here I show how to generate Wigner distribution for the vibrational ground state. To simplify the implementation, a simple form is used instead of Eq. (2.29) as

$$w_i(Q_i, P_i) = e^{-(Q_i^2 + P_i^2)}. \tag{2.31}$$

The sets of (Q_i, P_i) can be generated by rejection sampling as outlined in the following procedure:

1) Two random numbers Q_i and P_i are chosen uniformly from the interval [-3, 3] (This interval should be increased for high vibrational states).
2) A uniform random r_i number is generated from [0, 1].
3) Calculate w_i from Eq. (2.31) using (Q_i, P_i) obtained in 1).
4) If $w_i > r_i$, then Q_i and P_i are accepted; otherwise go back to 1).

This operation for generating the sets of (Q_i, P_i) is done for all vibrational modes.

The set of vibrational frequencies $\{\omega_i\}$ and the corresponding normal mode vectors $\{\boldsymbol{n}_i\}$ at the equilibrium structure $\boldsymbol{R}_{eq}$ can be calculated using quantum chemistry packages. The normal mode vectors $\{\boldsymbol{n}_i\}$ need to be provided in terms of mass-weighted Cartesian normal modes, in which an element n_i^α is defined as the product of the square root of the mass m^α of the atom and displacement x_i^α associated with Cartesian component α, as

$$n_i^\alpha = \sqrt{m^\alpha} x_i^\alpha. \tag{2.32}$$

A set of initial geometrical structure $\boldsymbol{R}$ and velocities of nuclei $\boldsymbol{v}$ is obtained by sum over all modes and given by [11],[14],[15]

$$R^\alpha = R_{eq}^\alpha + \sum_i Q_i \sqrt{\frac{\hbar}{m^\alpha \omega_i}} n_i^\alpha, \tag{2.33}$$

$$v^\alpha = \sum_i P_i \sqrt{\frac{\hbar \omega_i}{m^\alpha}} n_i^\alpha, \tag{2.34}$$

where R^α denote the element of the structure $\boldsymbol{R}$, v^α denote the element of velocity $\boldsymbol{v}$ and m^α is the mass of the atom associated with Cartesian component α.

2.1.3.2 Uniform random orientation

The orientation of a rigid body in a fixed space can be described using Euler angles which are introduced by Leonhard Euler [16]. In Euler angles, three times sequential rotation are denoted by three angles and there are twelve possible sequences of rotation axes. *z-x-z* type is used to generate uniform random orientation here. The original coordinates of the target grid body are denoted as x, y, z. The rotated coordinates are denoted as X, Y, Z and can be obtained as follows:

1) Rotate the coordinate system x, y, z about the z axis by ϕ. Then the new coordinate system x', y', z' is obtained.

2) Rotate the coordinate system x', y', z' about the x' axis by θ. Then the new coordinate system x'', y'', z'' is obtained.

3) Rotate the coordinate system x'', y'', z'' about the z'' axis by ψ. Then the rotated coordinate system X, Y, Z is obtained.

The rotation of the frame X, Y, Z from the frame of x, y, z can be represented by Euler angles (ϕ, θ, ψ), where

$$\phi \in [0, 2\pi)$$
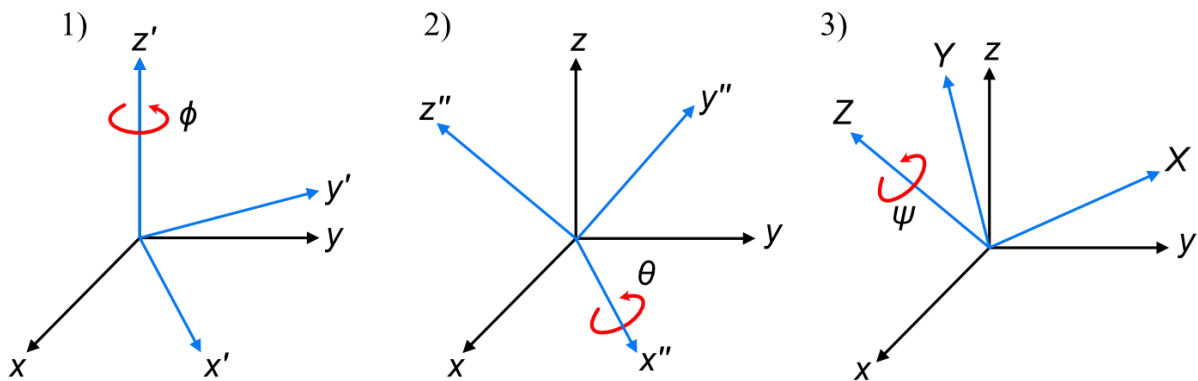$$\theta \in [0, \pi]$$
$$\psi \in [0, 2\pi). \tag{2.35}$$

Fig. 2.2: Operations in *z-x-z* Euler Angles.

For practical use, it is necessary to represent X, Y, Z in the original x, y, z frame. At the beginning, the rotation matrix $R_b(\alpha)$, which denotes the rotation about b axis by an angle α, is introduced. The rotation matrices for the rotation around x, y and z are given by

$$R_x(\alpha) = \begin{pmatrix} 1 & 0 & 0 \\ 0 & \cos\alpha & -\sin\alpha \\ 0 & \sin\alpha & \cos\alpha \end{pmatrix}, \tag{2.36}$$

$$R_y(\alpha) = \begin{pmatrix} \cos\alpha & 0 & \sin\alpha \\ 0 & 1 & 0 \\ -\sin\alpha & 0 & \cos\alpha \end{pmatrix}, \tag{2.37}$$

$$R_z(\alpha) = \begin{pmatrix} \cos\alpha & -\sin\alpha & 0 \\ \sin\alpha & \cos\alpha & 0 \\ 0 & 0 & 1 \end{pmatrix}. \tag{2.38}$$

The rotation operation around the x' axis can be expressed using $R_x(\theta)$ after reversely rotating about the z axis by ϕ, given as

$$R_{x'}(\theta) = R_z(\phi)R_x(\theta)R_z(-\phi). \tag{2.39}$$

In the same way as $R_{x'}(\theta)$, by using the fact $z' = z$, $R_{z''}(\psi)$ is given by

$$R_{z''}(\psi) = R_{x'}(\theta)R_z(\psi)R_{x'}(-\theta). \tag{2.40}$$

Finally, the rotation matrix $R(\phi, \theta, \psi)$ which represents the orientation denoted by Euler angles (ϕ, θ, ψ) can be written as

$$\begin{aligned} R(\phi, \theta, \psi) &= R_{z''}(\psi)R_{x'}(\theta)R_z(\phi) \\ &= [R_{x'}(\theta)R_z(\psi)R_{x'}(-\theta)]R_{x'}(\theta)R_z(\phi) \\ &= R_{x'}(\theta)R_z(\psi)R_z(\phi) \\ &= [R_z(\phi)R_x(\theta)R_z(-\phi)]R_z(\psi)R_z(\phi) \\ &= R_z(\phi)R_x(\theta)R_z(\psi). \end{aligned} \tag{2.41}$$

The rotation operation using $R(\phi, \theta, \psi)$ can be used to generate uniform orientated molecules. Here it should be noted that the transformation matrix is nonlinear in terms of the three angles ϕ, θ, ψ. Since the weights at $\theta \sim 0$ and $\theta \sim \pi$ is higher, the uniformly generated ϕ, θ, ψ do not form the uniform transformation. Therefore, to generate uniform orientated sampling, it is needed to reduce the weights at $\theta \sim 0$ and $\theta \sim \pi$.

The procedure is as follows [17]:

1) Choose three random numbers $u, v, w \in [0, 1]$.

2) Generate ϕ, θ, ψ as

$$\begin{aligned} \phi &= 2\pi u \\ \theta &= \arccos(2v - 1) \\ \psi &= 2\pi w. \end{aligned} \tag{2.42}$$

3) Rotate the molecule using $R(\phi, \theta, \psi) = R_z(\phi)R_x(\theta)R_z(\psi)$.

ϕ and ψ are uniformly chosen from the range of $[0, 2\pi]$. On the other hand, sine weighted distribution of θ is generated in the range of $[0, \pi]$ instead of uniform one. Here I show an example of uniform random orientation from a unit vector $\vec{r} = (1, 0, 0)$. 10000 random numbers for u, v, w are respectively generated in the range of $[0, 1]$. The distributions of the resulting ϕ, θ, ψ are shown in Fig. 2.3. For ϕ, ψ, the distributions are uniform in the range of $[0, 2\pi]$, whereas it has a sine shaped distribution for θ. Fig. 2.4 shows the generated points in the x, y, z frame by the rotation operations using $R_z(\phi)R_x(\theta)R_z(\psi)$. The points locate on the surface of a sphere of 1 radius which has its center at the origin. The distribution of the projections to x, y, z axes are uniform as shown in Fig. 2.5.
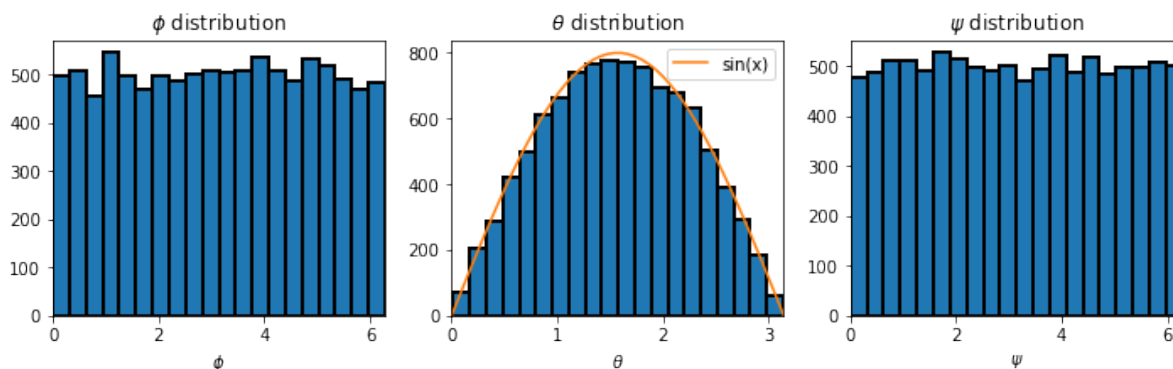
Fig. 2.3. The distribution of ϕ (left), θ (center), ψ (right) calculated from randomly generated u, v, w.

Fig. 2.4. The random generated points by the rotation operation of $R(\phi, \theta, \psi) = R_z(\phi)R_x(\theta)R_z(\psi)$ to $\vec{r} = (1, 0, 0)$.

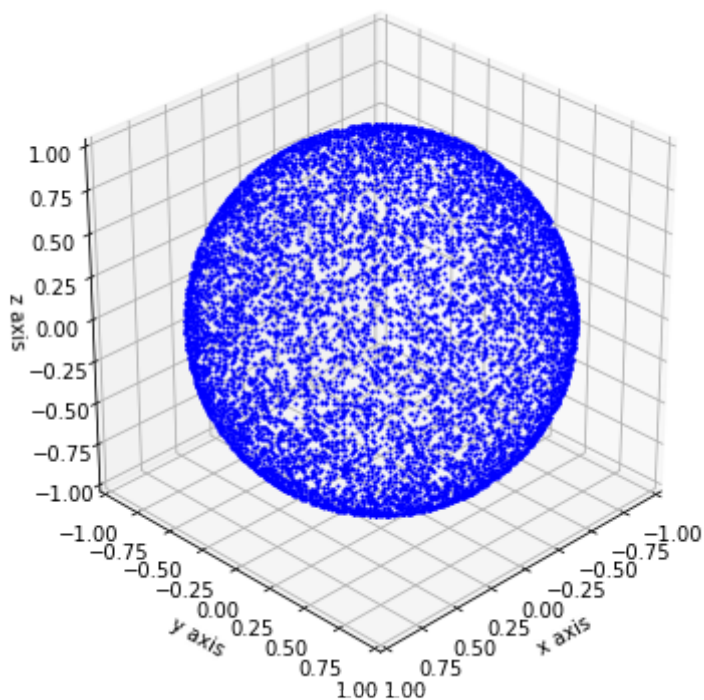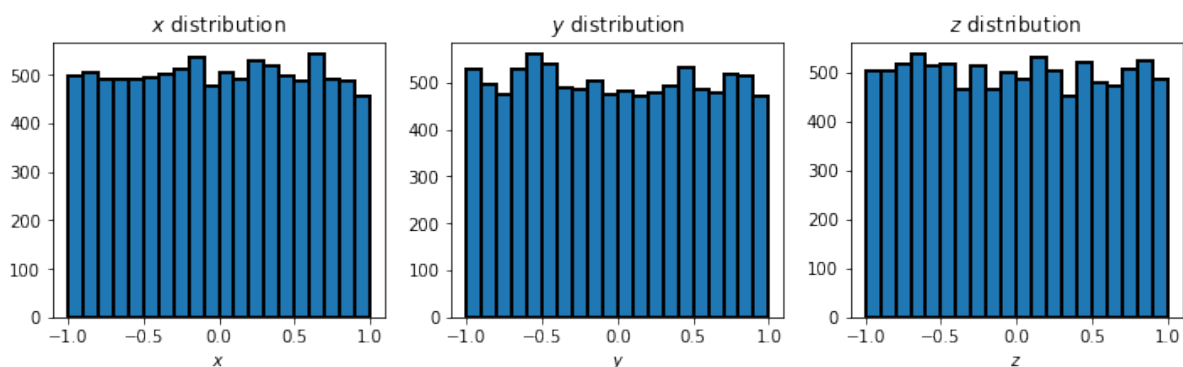Fig. 2.5. The distribution of X (left), Y (center), Z (right) of the points randomly generated by the rotation operation of $R(\phi, \theta, \psi) = R_z(\phi)R_x(\theta)R_z(\psi)$ to $\vec{r} = (1, 0, 0)$.

2.1.4 Velocity-Verlet algorithm

The time integration for Newton equation in Eq. (2.18) can be done using Velocity-Verlet algorithm [18], given by

$$R_I(t + \Delta t) = R_I(t) + v_I(t)\Delta t + \frac{F_I \Delta t^2}{2M}, \tag{2.43}$$

$$v_I(t + \Delta t) = v_I(t) + \frac{F_I(t) + F_I(t + \Delta t)}{2M_I}\Delta t, \tag{2.44}$$

where Δt is the time step for time evolution, M_I, R_I, v_I and F_I denote mass, positions, velocities and forces of the atomic nucleus I, respectively. This algorithm is known as a Symplectic integrator [19], which very nearly conserves the total energy and is particularly useful for long time simulations.

2.1.5 Data analysis

2.1.5.1 Identification of dissociation channels

A parent molecule may decompose to some fragments in the simulation under the intense field condition. In the results of *ab initio* molecular dynamics, the coordinates and velocities of nuclei in a molecular system at each time step can be obtained. The information of dissociation channels must be extracted from the coordinates of nuclei. Therefore, in order to obtain information of the dissociation channels for a lot of trajectories, it is needed a systematic method to check the dissociation channel of each trajectory. Here I introduce a technique based on ISM (Interpretive Structural Modeling) [20] in graph theory to identify the dissociation channel for each trajectory. Representing a molecule as a graph, atoms and bonds in a molecule are represented as vertices and edges, respectively. The fragments can be classified by checking the reachability in the graph. As the advantage of this method, it is easy to implement in a program code and available to extend to large molecular systems.

The procedure is as follows:

1) Number atoms as $(1,2, \ldots, i, j, \ldots, N)$.
2) Choose a threshold d to determine that there is a bond or not between two atoms, that is, to check the existence of the edge.
3) Calculate internuclear distance r_{ij} between atom i and atom j, where i and j run for 1 to N.
4) Make a matrix A in which element $a_{ij} = 1$ if $r_{ij} < d$; otherwise $a_{ij} = 0$. The diagonal element is $r_{ii} = 0$. A is called as adjacency matrix.

5) Calculate $T = (A + I)^{N-1}$, where I is identity matrix.

6) Check the elements t_{ij} in each row or column in T. If $t_{ij} > 0$, it means atom i and atom j are in a same moiety; if $t_{ij} = 0$, it means means atom i and atom j are in two different moieties.
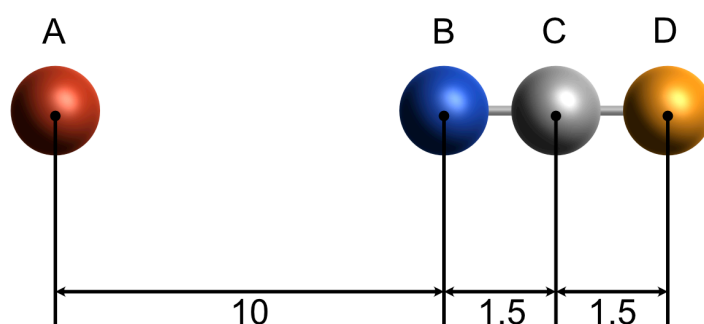
Fig. 2.6. Scheme of a virtual linear tetra-atomic molecule ABCD which decomposes into A + BCD. The internuclear distance between A and B, B and C, C and D are assumed to be 10, 1.5, 1.5, respectively.

Here a virtual tetra-atomic linear molecule ABCD, which decomposes into A and BCD, is taken as an example to show how this method works. As the first step, the atoms in ABCD can be numbered as A: 1, B: 2, C: 3, D: 4. Molecule A···BCD is assumed as linear and $r_{12} = 10, r_{23} = 1.5, r_{34} = 1.5$ as shown in Fig. 2.6. By choosing a threshold as $d = 2$, matrix A can be written as

$$A = \begin{pmatrix} 0 & 0 & 0 & 0 \\ 0 & 0 & 1 & 0 \\ 0 & 1 & 0 & 1 \\ 0 & 0 & 1 & 0 \end{pmatrix}. \tag{2.45}$$

$A + I$ is calculated as

$$A + I = \begin{pmatrix} 1 & 0 & 0 & 0 \\ 0 & 1 & 1 & 0 \\ 0 & 1 & 1 & 1 \\ 0 & 0 & 1 & 1 \end{pmatrix}. \tag{2.46}$$

Then T can be obtained as

$$T = (A + I)^3 = \begin{pmatrix} 1 & 0 & 0 & 0 \\ 0 & 4 & 5 & 3 \\ 0 & 5 & 7 & 5 \\ 0 & 3 & 5 & 4 \end{pmatrix}. \tag{2.47}$$

By checking the first row in T, that is, (1 0 0 0), it can be known that atom A has no connection with other atoms, namely, it is isolated. From the second row (0 4 5 3), the information that atoms B, C, D are in a same fragment can be obtained. Thus, the dissociation channel ABCD $\rightarrow$ A + BCD can be extracted by this method.

2.1.5.2 Momentum estimation of the fragment ion ejected through Coulomb explosion

After Coulomb explosion, the parent ion decomposes into fragment ions following the repulsive Coulombic potential energy surface. In order to compare with the momentum or kinetic energy of fragment ions observed in the experiments, it needs to know these values at an infinite internuclear distance in *ab initio* molecular dynamics calculation. However, it takes much time to carry out *ab initio* molecular dynamics calculation to obtain the kinetic energy and the momentum of fragment ions at a long internuclear distance. Here I show a method to estimate the kinetic energy and the momentum of fragment ions at an infinite internuclear distance.

In long internuclear distance range, a fragment ion is affected by Coulombic forces from other fragment ions. The potential energy of this fragment ion can be expressed using a virtual (or an effective) distance r as

$$U(r) = \frac{k}{r} + U_\infty, \qquad (2.48)$$

where k is a constant and U_∞ is the potential energy at $r = \infty$. The translational kinetic energy of this fragment ion can be written as

$$K(r) = \frac{a}{r} + K_\infty, \qquad (2.49)$$

where a is a constant and K_∞ is the translational kinetic energy of this fragment ion at $r = \infty$. The pairs of the translational kinetic energy $K(r)$ and the distance r can be calculated from the result of *ab initio* molecular dynamics and K_∞ can be obtained by fitting the function in Eq. (2.49) to these pairs of $(K(r), r)$. The momentum $\boldsymbol{P}_\infty$ at $r = \infty$ can be estimated by multiplied $\sqrt{K_\infty/K(r)}$ to the momentum $\boldsymbol{P}(r)$ at a certain distance r, as

$$\boldsymbol{P}_\infty = \sqrt{\frac{K_\infty}{K(r)}} \boldsymbol{P}(r). \qquad (2.50)$$

The procedure is as follows:

1) Take data sets with the length of l from the result of calculation.

2) Calculate the pairs of $(K(r), r)$ for the chosen data sets, where r is defined as the distance between the center of mass of the target fragment ion and that of the whole parent ion.

3) Fit function of Eq. (2.49) to $\{(K(r), r)\}$ and obtain K_∞.

4) $\boldsymbol{P}_\infty$ can be calculated using Eq. (2.50).

For example, the extraction of the translational kinetic energies of the fragment ions H^+ and OH^+ from one trajectory in the results of *ab initio* molecular dynamics calculation of H_2O^{2+} $\rightarrow H^+ + OH^+$ is shown here. The data sets with length of $l = 100$ were chosen for fitting. r was calculated as the distance between the center of mass of the fragment ion and that of the whole parent ion. The translational kinetic energies of H^+ and OH^+ as a function of r were fitted using Eq. (2.49) as shown in Fig. 2.7. The translational kinetic energies at $r = \infty$ were obtained as 5.9 eV for H^+ and 0.31 eV for OH^+.
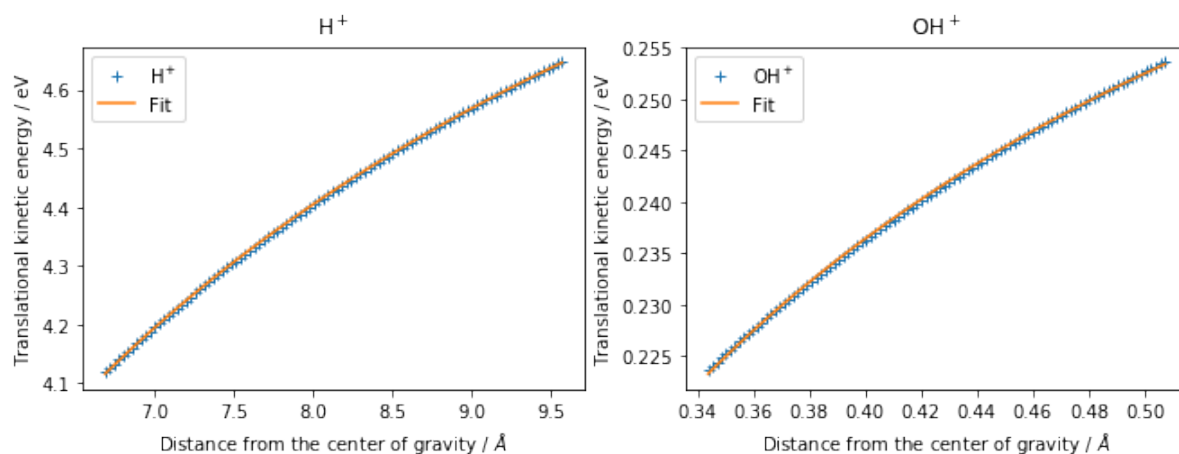
Fig. 2.7. Fitting for the translational kinetic energies of H^+(left) and OH^+(right) as a function of virtual (or an effective) distance r.

2.2 Time-dependent adiabatic state approach

2.2.1 Introduction

In order to describe the electronic and nuclear dynamics in intense laser fields, Sato *et al.* [21] proposed a description of dynamics in terms of "field-following" adiabatic states, that

is, time-dependent adiabatic state (TDAS) approach. They extended the concept of adiabatic state to the time region, that is, the electron motion follows the change of the time-dependent electric field. This approach is based on the approximation that the timescale of the change of electric field is much lower than that of electric motion. In TDAS approach, the effect of a laser field is included as the electric dipole interaction term into the electronic Hamiltonian. A TDAS $|n(r; R, t)\rangle$, characterized by the nuclear coordinate R and time t, is defined as an eigenstate of the instantaneous electronic Hamiltonian $\hat{H}_{el}(r; R, t)$ as

$$\hat{H}_{el}(r; R, t)|n(r; R, t)\rangle = E_n(R, t)|n(r; R, t)\rangle \tag{2.51}$$

with the eigenenergy $E_n(R, t)$, where the time-dependent instantaneous Hamiltonian is the sum of the field-free Hamiltonian and the scalar product of the dipole moment μ and the electric field $\varepsilon(t)$ as

$$\hat{H}_{el}(r; R, t) = \hat{H}_{el}(r; R) - \mu \cdot \varepsilon(t). \tag{2.52}$$

The eigenenergy $E_n(R, t)$ varies dependent on the electric field as shown in Fig. 2.8.
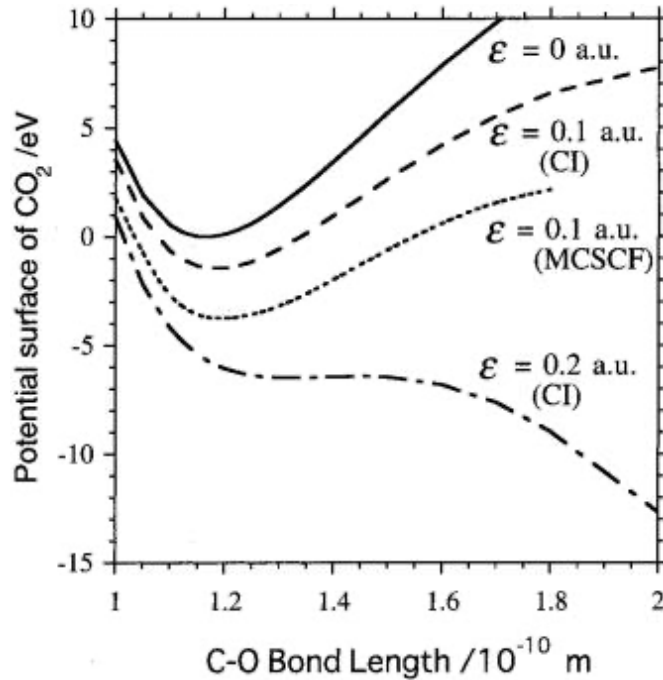
Fig. 2.8. Potential surfaces of the lowest adiabatic state of linear CO_2 at three electric field strengths (under symmetric stretching): $\varepsilon(t) = 0$ a.u. (solid line), the full valence configuration interaction (CI) calculation at $\varepsilon(t) = 0.1$ a.u. (broken), the multiconfiguration self-consistent field (MCSCF) calculation at $\varepsilon(t) = 0.1$ a.u. (dotted), and CI calculation at $\varepsilon(t) = 0.2$ a.u. (dash-dotted) [22].

2.2.2 Time evolution

The Hamiltonian of a molecular system is given by

$$\hat{H}(t) = \hat{H}_{el}(\boldsymbol{r}; \boldsymbol{R}, t) + \hat{T}(\boldsymbol{R}), \tag{2.53}$$

where $\hat{H}_{el}(\boldsymbol{r}; \boldsymbol{R}, t)$ is the instantaneous electronic Hamiltonian and $\hat{T}(\boldsymbol{R})$ is the nuclear kinetic energy operator, given by

$$\hat{T}(\boldsymbol{R}) = -\sum_I \frac{\hbar^2}{2M_I} \nabla_I^2. \tag{2.54}$$

The wavefunction is expressed as the linear combination of the products of the nuclear wavefunctions $\chi_n(R, t)$ and TDASs $|n(\boldsymbol{r}; \boldsymbol{R}, t)\rangle$, that is,

$$|\Psi(\boldsymbol{r}, \boldsymbol{R}, t)\rangle = \sum_n \chi_n(\boldsymbol{R}, t)|n(\boldsymbol{r}; \boldsymbol{R}, t)\rangle, \tag{2.55}$$

where $\chi_n(R, t)$ is the nuclear wavefunction. Substitution of Eq. (2.55) into the time-dependent Schrödinger equation

$$i\hbar \frac{\partial}{\partial t} |\Psi(\boldsymbol{r}, \boldsymbol{R}, t)\rangle = \hat{H}(t)|\Psi(\boldsymbol{r}, \boldsymbol{R}, t)\rangle, \tag{2.56}$$

yields

$$i\hbar \frac{\partial}{\partial t} \sum_n \chi_n(\boldsymbol{R}, t)|n(\boldsymbol{r}; \boldsymbol{R}, t)\rangle = \left(\hat{H}_{el}(\boldsymbol{r}; \boldsymbol{R}, t) + \hat{T}(\boldsymbol{R})\right) \sum_n \chi_n(\boldsymbol{R}, t)|n(\boldsymbol{r}; \boldsymbol{R}, t)\rangle. \tag{2.57}$$

Using the relationship in Eq. (2.51),

$$i\hbar \sum_n \left(\frac{\partial}{\partial t} \chi_n(\boldsymbol{R}, t)\right)|n(\boldsymbol{r}; \boldsymbol{R}, t)\rangle + i\hbar \sum_n \chi_n(\boldsymbol{R}, t)\left(\frac{\partial}{\partial t}|n(\boldsymbol{r}; \boldsymbol{R}, t)\rangle\right)$$

$$= \sum_n \chi_n(\boldsymbol{R}, t)E_n(\boldsymbol{R}, t)|n(\boldsymbol{r}; \boldsymbol{R}, t)\rangle + \sum_n \left(\hat{T}(\boldsymbol{R})\chi_n(\boldsymbol{R}, t)\right)|n(\boldsymbol{r}; \boldsymbol{R}, t)\rangle \tag{2.58}$$

Multiplying both side of Eq. (2.58) by $\langle m(\boldsymbol{r}; \boldsymbol{R}, t)|$,

$$i\hbar \frac{\partial}{\partial t} \chi_m(\boldsymbol{R}, t) = E_m(\boldsymbol{R}, t)\chi_m(\boldsymbol{R}, t) + \hat{T}(\boldsymbol{R})\chi_m(\boldsymbol{R}, t)$$

$$-i\hbar \sum_n \chi_n(\boldsymbol{R}, t)\langle m(\boldsymbol{r}; \boldsymbol{R}, t)|\frac{\partial}{\partial t}|n(\boldsymbol{r}; \boldsymbol{R}, t)\rangle \tag{2.59}$$

To calculate the nonadiabatic term $\langle m(\boldsymbol{r}; \boldsymbol{R}, t)|\frac{\partial}{\partial t}|n(\boldsymbol{r}; \boldsymbol{R}, t)\rangle$, we start from the differential of Eq. (2.51) by time t, as

$$\frac{\partial}{\partial t}\left(\hat{H}_{el}(\boldsymbol{r}; \boldsymbol{R})|n(\boldsymbol{r}; \boldsymbol{R}, t)\rangle\right) = \frac{\partial}{\partial t}(E_n(\boldsymbol{R}, t)|n(\boldsymbol{r}; \boldsymbol{R}, t)\rangle). \tag{2.60}$$

After rearranging this equation, it yields

$$\left(\frac{\partial}{\partial t}\widehat{H}_{el}(\boldsymbol{r};\boldsymbol{R})\right)|n(\boldsymbol{r};\boldsymbol{R},t)\rangle + \widehat{H}_{el}(\boldsymbol{r};\boldsymbol{R})\left(\frac{\partial}{\partial t}|n(\boldsymbol{r};\boldsymbol{R},t)\rangle\right)$$
$$= \left(\frac{\partial}{\partial t}E_n(\boldsymbol{R},t)\right)|n(\boldsymbol{r};\boldsymbol{R},t)\rangle + E_n(\boldsymbol{R},t)\frac{\partial}{\partial t}|n(\boldsymbol{r};\boldsymbol{R},t)\rangle. \tag{2.61}$$

Multiplying both side of this equation by $\langle m(\boldsymbol{r};\boldsymbol{R},t)|$, it yields

$$\langle m(\boldsymbol{r};\boldsymbol{R},t)|\left(\frac{\partial}{\partial t}\widehat{H}_{el}(\boldsymbol{r};\boldsymbol{R})\right)|n(\boldsymbol{r};\boldsymbol{R},t)\rangle + E_m(\boldsymbol{R},t)\langle m(\boldsymbol{r};\boldsymbol{R},t)|\left(\frac{\partial}{\partial t}|n(\boldsymbol{r};\boldsymbol{R},t)\rangle\right)$$
$$= E_n(\boldsymbol{R},t)\langle m(\boldsymbol{r};\boldsymbol{R},t)|\frac{\partial}{\partial t}|n(\boldsymbol{r};\boldsymbol{R},t)\rangle. \tag{2.62}$$

Finally, the field-induced nonadiabatic coupling can be calculated as

$$\langle m(\boldsymbol{r};\boldsymbol{R},t)|\frac{\partial}{\partial t}|n(\boldsymbol{r};\boldsymbol{R},t)\rangle = \frac{\langle m(\boldsymbol{r};\boldsymbol{R},t)|\left(\frac{\partial}{\partial t}\widehat{H}_{el}(\boldsymbol{r};\boldsymbol{R})\right)|n(\boldsymbol{r};\boldsymbol{R},t)\rangle}{E_n(\boldsymbol{R},t) - E_m(\boldsymbol{R},t)}$$
$$= \frac{\langle m(\boldsymbol{r};\boldsymbol{R},t)|\left(\frac{\partial}{\partial t}(-\boldsymbol{\mu}(\boldsymbol{r},\boldsymbol{R},t)\cdot\boldsymbol{\varepsilon}(t))\right)|n(\boldsymbol{r};\boldsymbol{R},t)\rangle}{E_m(\boldsymbol{R},t) - E_n(\boldsymbol{R},t)}$$
$$= \frac{\langle m(\boldsymbol{r};\boldsymbol{R},t)|\boldsymbol{\mu}(\boldsymbol{r},\boldsymbol{R},t)|n(\boldsymbol{r};\boldsymbol{R},t)\rangle}{E_m(\boldsymbol{R},t) - E_n(\boldsymbol{R},t)}\frac{d\boldsymbol{\varepsilon}(t)}{dt}. \tag{2.63}$$

Let this term be denoted as

$$N_{mn} \equiv \frac{\langle m(\boldsymbol{r};\boldsymbol{R},t)|\boldsymbol{\mu}(\boldsymbol{r},\boldsymbol{R},t)|n(\boldsymbol{r};\boldsymbol{R},t)\rangle}{E_m(\boldsymbol{R},t) - E_n(\boldsymbol{R},t)}\frac{d\boldsymbol{\varepsilon}(t)}{dt}. \tag{2.64}$$

Thus, the time evolution can be rewritten in the matrix expression as

$$i\hbar\frac{\partial}{\partial t}\begin{pmatrix}\chi_1(\boldsymbol{R},t)\\\chi_2(\boldsymbol{R},t)\\\chi_3(\boldsymbol{R},t)\\\vdots\end{pmatrix} = \left(-\sum_I\frac{\hbar^2}{2M_I}\nabla_I^2\,\mathbf{I} + \begin{pmatrix}E_1 & N_{12} & N_{13} & \cdots\\N_{21} & E_2 & N_{23} & \cdots\\N_{31} & N_{32} & E_3 & \cdots\\\vdots & \vdots & \vdots & \ddots\end{pmatrix}\right)\begin{pmatrix}\chi_1(\boldsymbol{R},t)\\\chi_2(\boldsymbol{R},t)\\\chi_3(\boldsymbol{R},t)\\\vdots\end{pmatrix}, \tag{2.65}$$

where $\mathbf{I}$ is the identity matrix.

2.2.3 *Ab initio* molecular dynamics combined with TDAS approach

The classical trajectories can be calculated instead of the nuclear wavepacket on the potential energy surface of TDAS in *ab initio* molecular dynamics. In the adiabatic picture, the classical nuclear motion on the nth TDAS $|n(\boldsymbol{r};\boldsymbol{R},t)\rangle$ is given by

$$M_I \frac{d^2 \boldsymbol{R}_I}{dt^2} = -\nabla_I E_n(\boldsymbol{R}, t), \tag{2.66}$$

where M_I and $\boldsymbol{R}_I$ are the mass and the coordinates of the Ith nucleus, respectively. The potential energy $E_n(\boldsymbol{R}, t)$ is obtained from

$$\widehat{H}_{el}(\boldsymbol{r}; \boldsymbol{R}, t)|n(\boldsymbol{r}; \boldsymbol{R}, t)\rangle = E_n(\boldsymbol{R}, t)|n(\boldsymbol{r}; \boldsymbol{R}, t)\rangle. \tag{2.67}$$

This calculation can be done using molecular orbital package programs with applying a static electric field at each time step.

2.3 Time-dependent configuration interaction

2.3.1 Introduction

In intense laser fields, the strong interaction of the light field and molecules can induce various characteristic phenomena. For larger systems, some approximations are needed to describe the light-matter interaction. To treat many-body electronic dynamics in intense fields, the time-dependent Schrödinger equation can be calculated based on the molecular orbital approach. This method is called time-dependent configuration interaction (TD-CI) [23]–[27] where the laser effect is included as the electric dipole interaction. The eigenenergy and the transition dipole matrix elements can be calculated using molecular orbital package programs.

2.3.2 Time evolution

The time-dependent Schrödinger equation with the semi-classical electric dipole approximation for the electronic wavefunction $\Psi(t)$ is given by

$$i\hbar \frac{\partial}{\partial t} \Psi(t) = [H_{el} - \boldsymbol{\mu} \cdot \boldsymbol{\varepsilon}(t)]\Psi(t), \tag{2.68}$$

where H_{el} is the field-free electric Hamiltonian, $\boldsymbol{\mu} \cdot \boldsymbol{E}(t)$ is the dipole coupling term which consists of the electric dipole moment $\boldsymbol{\mu}$ and the electric field $\boldsymbol{\varepsilon}(t)$. The electronic wavefunction $\Psi(t)$ is written as the linear combination of the eigenfunction ϕ_n of H_{el} with the eigenenergy E_n, as

$$\Psi(t) = \sum_n C_n(t)\phi_n, \tag{2.69}$$

$$H_{el}\phi_n = E_n\phi_n. \tag{2.70}$$

Substituting Eq. (2.69) into Eq. (2.68), we obtain

$$i\hbar \frac{\partial}{\partial t} \sum_n C_n(t)\phi_n = [H_{el} - \boldsymbol{\mu} \cdot \boldsymbol{\varepsilon}(t)] \left(\sum_n C_n(t)\phi_n \right)$$

$$= \sum_n C_n(t)E_n\phi_n - \sum_n C_n(t)\boldsymbol{\mu} \cdot \boldsymbol{\varepsilon}(t)\phi_n. \tag{2.71}$$

Multiplying both side of this equation by $^*\phi_m$ and integrating over the whole space, it yields

$$i\hbar \frac{\partial}{\partial t} C_m(t) = E_m C_m(t) - \sum_n \boldsymbol{\mu}_{mn} \cdot \boldsymbol{\varepsilon}(t) C_n(t), \tag{2.72}$$

where $\boldsymbol{\mu}_{mn}$ is the transition dipole matrix element, given by

$$\boldsymbol{\mu}_{mn} \equiv \langle \phi_m | \boldsymbol{\mu} | \phi_n \rangle. \tag{2.73}$$

The time propagation of the coefficient vector $\boldsymbol{C}(t)$ can be carried out by using a split operator technique [28] with

$$\boldsymbol{C}(t + \Delta t) = \left[\prod_{q=x,y,z} \boldsymbol{U}_q^\dagger e^{i\mu_q \varepsilon_q(t)\Delta t} \boldsymbol{U}_q \right] e^{-iH_{el}\Delta t} \boldsymbol{C}(t), \tag{2.74}$$

where $\boldsymbol{U}_q$ ($q = x, y, z$) is a unitary matrix describing the transformation between the eigenstate basis set and the basis set in which the dipole matrix $\boldsymbol{\mu}_q$ is diagonal.

Reference

[1] M. Born and R. Oppenheimer, *Ann. Phys.* **389**, 457 (1927).

[2] R. Car and M. Parrinello, *Phys. Rev. Lett.* **60**, 204 (1988).

[3] D.K. Remler and P.A. Madden, *Mol. Phys.* **70**, 921 (1990).

[4] M.E. Tuckerman, P.J. Ungar, T. Von Rosenvinge, and M.L. Klein, *J. Phys. Chem.* **100**, 12878 (1996).

[5] M.E. Tuckerman, *J. Phys. Condens. Matter* **14**, 1297 (2002).

[6] K. Laasonen, *Methods Mol. Biol.* **924**, 29 (2013).

[7] D. Marx, *An Introduction to Ab Initio Molecular Dynamics Simulations* (John von Neumann Institute for Computing, Jülich, NIC Series, 2006).

[8] E. Wigner, *Phys. Rev.* **40**, 749 (1932).

[9] S. Goursaud, M. Sizun, and F. Fiquet-Fayard, *J. Chem. Phys.* **65**, 5453 (1976).

[10] E.J. Heller, *J. Chem. Phys.* **65**, 1289 (1976).

[11] L. Sun and W.L. Hase, *J. Chem. Phys.* **133**, 044313 (2010).

[12] J.P. Dahl and M. Springborg, *J. Chem. Phys.* **88**, 4535 (1988).

[13] J. von Neumann, in *Monte Carlo Method*, edited by A.S. Householder, G.E. Forsythe, and H.H. Germond (US Government Printing Office, Washington, DC, 1951), pp. 36–38.

[14] S.Y.Y. Wong, D.M. Benoit, M. Lewerenz, A. Brown, and P.N. Roy, *J. Chem. Phys.* **134**, 1 (2011).

[15] M.K. Ganesa Subramanian, R. Santra, and R. Welsch, *Phys. Rev. A* **98**, 063421 (2018).

[16] L. Euler, *Novi Comment. Acad. Sci. Petropolitanae* **20**, 189 (1776).

[17] X. Perez-Sala, L. Igual, S. Escalera, and C. Angulo, in *Robot. Vis.* (IGI Global, 2012), pp. 23–42.

[18] L. Verlet, *Phys. Rev.* **159**, 98 (1967).

[19] D. Donnelly and E. Rogers, *Am. J. Phys.* **73**, 938 (2005).

[20] J.N. Warfield, *IEEE Trans. Syst. Man Cybern.* **4**, 405 (1974).

[21] Y. Sato, H. Kono, S. Koseki, and Y. Fujimura, *J. Am. Chem. Soc.* **125**, 8019 (2003).

[22] H. Kono, S. Koseki, M. Shiota, and Y. Fujimura, *J. Phys. Chem. A* **105**, 5627 (2001).

[23] P. Krause, T. Klamroth, and P. Saalfrank, *J. Chem. Phys.* **123**, 1 (2005).

[24] H.B. Schlegel, S.M. Smith, and X. Li, *J. Chem. Phys.* **126**, 244110 (2007).

[25] F. Remacle, R. Kienberger, F. Krausz, and R.D. Levine, *Chem. Phys.* **338**, 342 (2007).

[26] L. Greenman, P.J. Ho, S. Pabst, E. Kamarchik, D.A. Mazziotti, and R. Santra, *Phys. Rev. A* **82**, 023406 (2010).

[27] T. Klamroth, *J. Chem. Phys.* **124**, 144310 (2006).

[28] T. Klamroth, *Phys. Rev. B* **68**, 245421 (2003).

Chapter 3.

Dissociation and ionization dynamics of water molecule in intense laser fields

Abstract

In order to investigate dissociation dynamics of water molecules in a near-IR femtosecond intense laser pulse, we performed *ab initio* molecular dynamics calculations combined with the time-dependent adiabatic state approach. We showed that H^+ is produced from H_2O^{2+} not only by the two-body dissociation but also by the three-body dissociation and that the kinetic energy distributions of H^+ for the two-body dissociation are in good agreement with the corresponding experimental data. We also performed time-dependent configuration interaction calculations to estimate the ionization probability of H_2O^{2+} and confirmed that H_2O^{2+} is ionized to H_2O^{3+} by the charge-resonance enhanced ionization mechanism.

3.1   Introduction

When molecules are exposed to an intense laser field, they are strongly coupled with the light field and their structural deformation and bond breaking processes are governed by the light-dressed potential energy surfaces as long as the temporal variation of the electric field of light is slow enough so that electrons follow it adiabatically [1]–[5]. In the early studies of the Coulomb explosion processes of linear and bent triatomic molecules [6],[7], proceeding after molecules are multiply ionized by an intense femtosecond laser field, it was shown that the geometrical structure of molecules can vary to a large extent through the interaction with the light field.

In order to understand theoretically this structural deformation of molecules in a femtosecond laser field, we need to consider not only the interaction of neutral molecules with the light field but also the interaction of the singly and multiply charged molecules with the light field because the ionization proceeds within the femtosecond laser field. However, it has been a difficult task to treat theoretically this complex process in which the charge number of

40

molecules increases within the laser field while the structural deformation proceeds simultaneously.

In the present study, we investigate theoretically the interaction of a water molecule (H_2O), one of the simplest triatomic molecules, with an intense near-IR femtosecond laser field by treating explicitly the interactions of H_2O, H_2O^+, H_2O^{2+}, and H_2O^{3+} with the laser field and examine if the released kinetic energies of H^+ (a proton) produced after the fragmentation processes can consistently reproduce those obtained by previous experimental studies.

Two decades ago, the Coulomb explosion of multiply charged water molecules created by the irradiation of near-IR intense laser pulses were investigated by Sanderson et $al.$ [8] and Liu et $al.$ [9]. Sanderson et $al.$ [8] used laser pulses whose parameters are $\lambda = 790$ nm, $\Delta t = 50$ fs, and $I = 3 \times 10^{16}$ W/cm^2 while Liu et $al.$[5] used laser pulses whose parameters are $\lambda = 800$ nm, $\Delta t = 100$ fs, and $I = 1.2 \times 10^{15}$ W/cm^2, where λ, Δt, and I denote respectively the wavelength, pulse duration, and the peak laser-field intensity. Both of these groups found that the O-H distance increases and the H-O-H angle becomes larger by the time when multiply charged water molecules are created within the laser field. Later, in 2005, Légaré et $al.$ [10] investigated the structural deformation of D_2O using much shorter laser pulses whose laser parameters are $\lambda = 800$ nm, $\Delta t = 8$ fs, and $I = \sim 5 \times 10^{15}$ W/cm^2 and showed that the structural deformation of D_2O hardly occurs when D_2O^{4+} is created within the 8-fs laser pulse.

In 2006, Nakano et $al.$ [11] recorded the momentum distributions of H^+ ejected from H_2O ionized by the irradiation of near-IR ($\lambda = 800$ nm) laser pulses ($\Delta t = 8$ fs and $I = 1.6 \times 10^{15}$ W/cm^2; $\Delta t = 20$ fs and $I = 0.64 \times 10^{15}$ W/cm^2). They found in the momentum distribution of H^+ that a peak appearing at 32.4×10^3 u m/s (corresponding to the kinetic energy of 5.40 eV) at $\Delta t = 8$ fs increases only slightly to 32.6×10^3 u m/s (5.47 eV) when Δt is changed to 20 fs. They also found that a peak appearing at 45.8×10^3 u m/s (10.8 eV) at $\Delta t = 8$ fs decreases largely to 41.6×10^3 u m/s (8.90 eV) when Δt is changed to 20 fs. On the basis of this characteristic difference in the dependences of the momentum release on the laser pulse duration, they suggested that the peak at ~ 5.4 eV can be assigned to H^+ ejected from H_2O^{2+} by the two-body Coulomb explosion; $H_2O^{2+} \rightarrow H^+ + OH^+$, and that a peak appearing above 8 eV can be assigned to H^+ ejected from the three-body Coulomb explosion of H_2O^{3+}; $H_2O^{3+} \rightarrow H^+ + O^+ + H^+$.

In 2015, Liu et $al.$ [12] irradiated water molecules with near-IR ($\lambda = 800$ nm) shorter ($\Delta t = 7$ fs and $I = 1.6 \times 10^{15} - 3.0 \times 10^{15}$ W/cm^2) and longer ($\Delta t = 25$ fs and $I = 1.2 \times 10^{15} - 2.1 \times 10^{15}$ W/cm^2) femtosecond laser pulses and detected the fragment ions in coincidence to investigate the three-body Coulomb explosion of H_2O^{3+} and H_2O^{4+}. For the three-body Coulomb explosion of H_2O^{3+}, $H_2O^{3+} \rightarrow H^+ + O^+ + H^+$, they showed that a peak in the kinetic energy distribution appearing in the range of 10-12 eV at $\Delta t = 7$ fs decreased by about 2 eV when the pulse duration was changed to 25 fs, which is consistent with the dependence of the kinetic energy of H^+ on the pulse duration reported by Nakano et $al.$ [11]. Therefore, as long as the peak laser field intensity of near-IR laser pulses is in the range of $1 \times 10^{15} < I < 2 \times 10^{15}$ W/cm^2, a peak in the kinetic energy distribution of H^+ is located at around 11 eV when $\Delta t = 7$-8 fs and at around 9 eV when $\Delta t = 20$-25 fs.

In the following sections, we will examine if these assignments made based on the experimental results can be supported by theoretical calculations in which the interaction with an intense laser field is explicitly included at the respective charge states of H_2O. First, we perform ab $initio$ molecular dynamics calculations combined with the time-dependent adiabatic state approach [13] to treat the nuclear dynamics of H_2O^+ on the time-dependent adiabatic state (TDAS) potential prior to the ionization to H_2O^{2+} and that of H_2O^{2+} on the TDAS, from which we derive the kinetic energy distribution of H^+ produced from H_2O^{2+}. Then, we perform time-dependent configuration interaction calculations to estimate the ionization probability of H_2O^{2+} to H_2O^{3+} in order to clarify the role of the enhanced ionization process [14],[15], which has been considered as the mechanism by which the kinetic energy of H+ becomes smaller when Δt increases [12],[16].

3.2   Results and discussion

3.2.1   Coulomb explosion of H_2O^{2+}

In order to mimic the experimental conditions of Ref. [11], we calculate the TDASs of H_2O, H_2O^+ and H_2O^{2+} in the presence of a linearly polarized near-IR ($\lambda = 800$ nm) laser electric field for the two different sets of laser parameters; $(\Delta t, I) = (8$ fs, 1.6×10^{15} W/cm^2) and (20 fs, 0.64×10^{15} W/cm^2) by the complete active space self-consistent field (CASSCF) [17] method with the basis set of 6-311+G(d,p) implemented in the Gaussian 09 package [18]. The CASSCF

active space contains all 6 valence molecular orbitals composed of the $2s$, $2p$ atomic orbitals for O and 1s for H [19]. We perform the calculations using the larger basis set, "aug-cc-pVTZ" and "the basis set consisting of aug-cc-pVQZ for oxygen and aug-cc-pVTZ for hydrogen," and confirm that the precision of the calculations with the 6-311+G(d,p) basis set is sufficiently high.

We assume that the laser pulses have a Gaussian envelope with a sine-type wave form, that is, the carrier envelope phase is $\pi/2$. We also assume that the laser polarization direction is parallel to the line connecting the two H atoms in H_2O, which is parallel to the molecular b-axis, because we find no three-body dissociation proceeds when the laser polarization direction is set to be parallel to the a-axis or to the c-axis.

We set the $t = 0$ at the temporal center of the laser pulses and start the classical trajectory calculations from $t = -20$ fs for the 8 fs pulse and from $t = -50$ for the 20 fs pulse with neutral H_2O prepared at the equilibrium geometrical structure in the electronic ground state obtained at the CASSCF level. We create a set of 100 molecular geometries and velocities using harmonic-oscillator Wigner distributions for the respective three vibrational modes in the vibrational ground state [20] and run the trajectories on the TDAS for the period of 500 fs with a time step of 0.1 fs. We solve the Newton's equation by the velocity-Verlet method.
In the course of the calculation, we change the TDAS from the lowest-energy TDAS of neutral H_2O to the lowest-energy TDAS of H_2O^+ when the laser field intensity exceeds 1×10^{13} W/cm^2, corresponding to the appearance laser field intensity of H_2O^+ (Ref. [21]), reflecting the fact that the ionization to cation proceeds in the leading edge of the laser pulse. We adopt this model of single ionization timing because the geometrical structures of H_2O and H_2O^+ are close to each other under the 8 fs and 20 fs laser pulses, and consequently, the ionization timing has only little effect on the dynamics in the later stage.

We then change the TDAS to the lowest-energy TDAS of H_2O^{2+} at the timings within the laser pulse when the amplitude of the electric field of light takes the local maxima whose field intensity exceeds 10^{14} W/cm^2. The number of the timings for the 8 fs laser pulse is 12 and that for the 20 fs laser pulse is 24. At each timing of the double ionization, the trajectories on the lowest-energy TDAS of H_2O^+ start running on the lowest-energy TDAS of H_2O^{2+}. It is assumed that the velocities of the nuclei do not change at the timings of the change in the charge states, that is, at the timings of the switching from neutral to cation and the switching

from cation to dication. In the course of the trajectory calculations, we judge that the dissociation is completed when one of the O-H distances exceeds 15 Å.

In order to derive the kinetic energy of the H^+ fragment, we calculate the distribution $K(R)$ of the kinetic energy of H^+ with respect to the center of gravity of the entire molecule as a function of the distance R between H^+ and the center of gravity, and fit the results to the formula,

$$K(R) = \frac{a}{R} + K_\infty, \qquad (1)$$

where a is a constant and K_∞ represents the kinetic energy of the H^+ fragment ejected from the Coulomb explosion.

In the MD simulation, we find that H_2O^{2+} decomposes through the following two dissociation channels; the two-body dissociation,

$$H_2O^{2+} \rightarrow H^+ + OH^+, \qquad (2)$$

and the three-body dissociation,

$$H_2O^{2+} \rightarrow H^+ + O + H^+. \qquad (3)$$

For the 8 fs pulse, the kinetic energy distributions obtained for the 12 timings of the ionization from H_2O^+ and H_2O^{2+} are summed up with equal weights, and for the 20 fs pulse, those obtained for the 24 timings. The results are shown in Figs. 3.1(a) and 3.1(b) for the 8 fs pulse and the 20 fs pulse, respectively.

In the kinetic energy distribution of the two-body dissociation channel (2), a single peak appears at 5.5 eV (32.7×10^3 u ms^{-1}) for the 8 fs pulse and at 5.7 eV (33.3×10^3 u ms^{-1}) for the 20 fs pulse excitation. The kinetic energy values of these peak positions are in good agreement with the experimental momentum distributions of H^+ reported in Ref. [11] in which a peak appears at 32.4×10^3 u ms^{-1} (5.40 eV) for the 8 fs pulse and 32.6×10^3 u ms^{-1} (5.47 eV) for the 20 fs pulse excitation, which confirmed the assignment of the corresponding peak profile in the experimental kinetic energy distributions in the previous studies (Ref. [22]) to the two-body dissociation of D_2O^{2+}; $D_2O^{2+} \rightarrow D^+ + OD^+$.
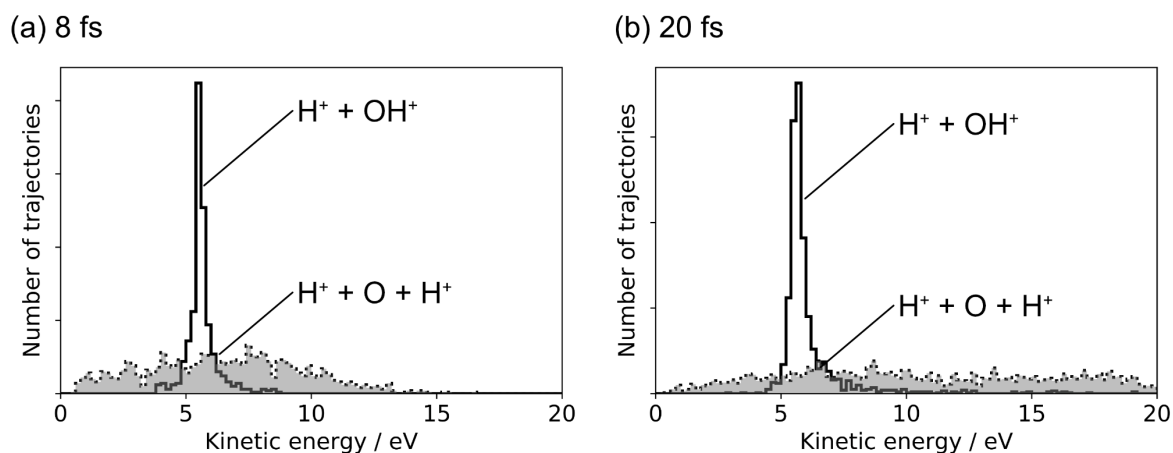
(a) 8 fs

(b) 20 fs

Fig. 3.1. The kinetic energy distributions of H^+ ejected from H_2O^{2+} via the two-boy dissociation channel (solid line: $H_2O^{2+} \rightarrow H^+ + OH^+$) and via the three-body dissociation channel (dotted line: $H_2O^{2+} \rightarrow H^+ + O + H^+$) obtained when H_2O starts interacting with near-IR ($\lambda = 800$ nm) laser pulses whose pulse durations and peak light-field intensities are (a) 8-fs and 1.6×10^{15} W/cm^2 and (b) 20-fs and 0.64×10^{15} W/cm^2.

It can be seen commonly in Figs. 3.1(a) and 3.1(b) that the kinetic energy distribution of the three-body dissociation channel (3), $H_2O^{2+} \rightarrow H^+ + O + H^+$, exhibit a broad structure. The broad structure for the 8 fs laser pulse covers the range of 0.5-15 eV (10–54×10^3 u ms^{-1}) and that for the 20 fs laser pulse covers the range of 0.5-20 eV (10–62×10^3 u ms^{-1}). Therefore, the broad baseline structure appearing in the experimental data in the range of 10-62×10^3 u ms^{-1} reported before (Ref. [11]) can be assigned to the three-body dissociation of H_2O^{2+}.

Next, we examine the effect of the timings of the ionization from H_2O^+ to H_2O^{2+}. In Figs. 3.2(a) and 3.2(b), we show respectively the kinetic energy distribution of H^+ ejected from H_2O^{2+} through the two-body dissociation channel at the 12 ionization timings and through the three-body dissociation channels at the 24 ionization timings.

It can be seen in both 8 fs and 20 fs cases that, in the earlier part of the laser pulse, the three-body dissociation dominates the two-body dissociation and the distribution for the three-body dissociation shifts toward the lower kinetic energy side as the ionization occurs at the later timing. On the other hand, in both 8 fs and 20 fs cases, the two-body dissociation dominates in the later part of the laser pulse and the peak profile of the two-body dissociation exhibits almost the same position at around 5.5 eV (33×10^3 u ms^{-1}).

The kinetic energy distributions of H^+ can be influenced by the depletion associated with the further ionization to H_2O^{3+} and by the ionization rate to H_2O^{2+}, both of which may vary depending on the ionization timing. Even though we did not take into account these two effects, the resultant kinetic energy distributions are in good agreement with the experimental results, suggesting that these two effects may not be significantly large.
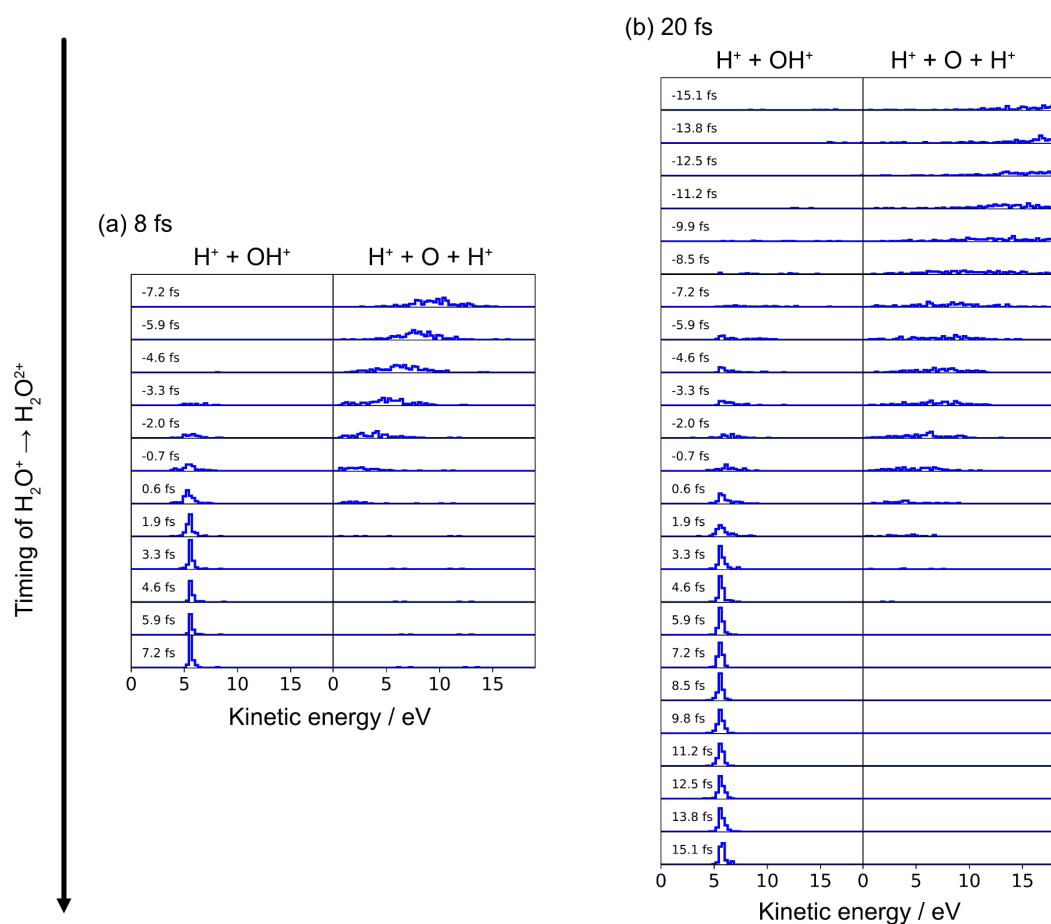

Fig. 3.2. The kinetic energy distributions of H^+ ejected through the two-body and three-body dissociation of H_2O^{2+} at the different timings of the ionization from H_2O^+ to H_2O^{2+} for the 8 fs pulse (a) and the 20-fs pulse (b). The numbers shown on the left side of each frame are the ionization timings.

In order to interpret the dependences of the kinetic energy distributions on the ionization timing shown in Fig. 3.2, we examine the structural deformation in the stages of H_2O and H_2O^+ until the timing of the ionization to H_2O^{2+}. In Fig. 3.3, the length of one of the two O-H bonds of H_2O and H_2O^+ is shown as a function of time for the 8 fs and 20 fs cases. In the case of the 8 fs pulse shown in Fig. 3.3(a), except five trajectories exhibiting the dissociation into $H + OH^+$, the O-H bond length shows the oscillation in the range of 0.9-1.5 Å. In the case of the 20 fs pulse shown in Fig. 3.3(b), no dissociating trajectories are found and the O-H bond length shows the oscillation in the range of 0.9-1.3 Å. These results show that the O-H bond length of H_2O^+ oscillates within the molecular domain and that the dissociation does not proceed by the irradiation of the 8 fs or 20 fs intense laser pulse except the minor dissociation into $H + OH^+$ appearing only in the 8 fs case.
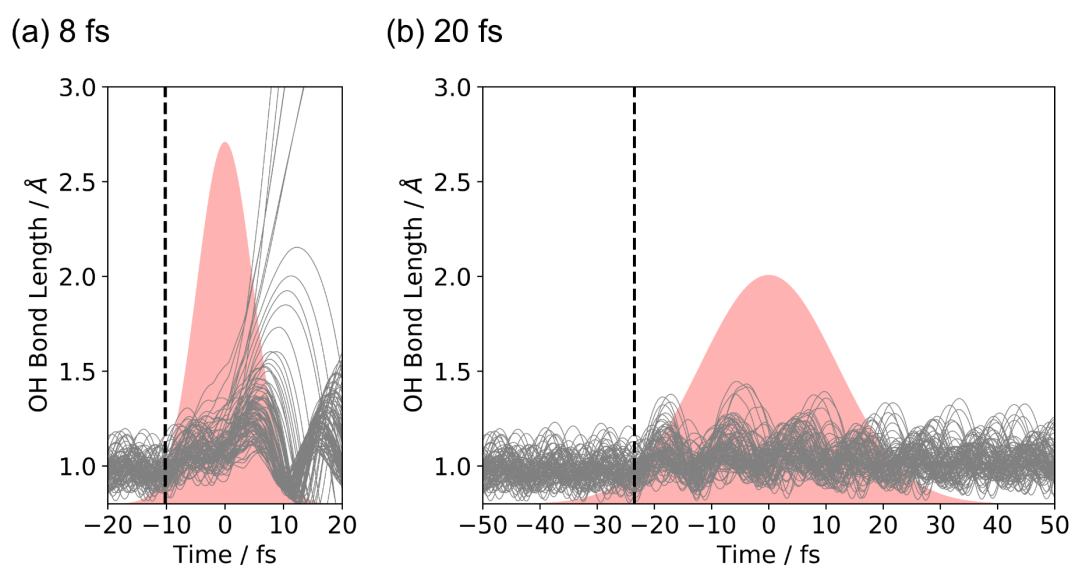

Fig. 3.3. The O-H bond length of H_2O and H_2O^+ as a function of time for the 8 fs pulse (a) and 20 fs pulse (b). The vertical broken line shows the timing of the ionization from H_2O to H_2O^+. The shaded area in each frame shows the envelope of the laser pulse. We start calculations from t = -20 for the 8 fs pulse and from t = -50 for the 20 pulse.

Because the structural changes in H_2O^+ is found to be small and H_2O^+ stays in the molecular domain during the period of the interaction with the intense laser field, the origin of the variation in the kinetic energy distributions as a function of the ionization timing shown in Fig. 3.2 for the three-body dissociation channel can be ascribed to the variation in the time-dependent adiabatic surface (TDAS) of a dication, H_2O^{2+}, as explained below.

In Fig. 3.4, the variation of the O-H distance in the course of the three-body dissociation into $H^+ + O + H^+$ is shown after the dication, H_2O^{2+} is created at the three different ionization timings at -13.8, -7.2, and -0.7 fs, within the 20 fs laser field. As shown in Fig. 3.4(a), if the ionization timing is -13.8 fs, the O-H distance increases to reach around 2.0 Å by the time when the light field intensity becomes maximum at $t = 0$ fs. In the time zone around the maximum intensity, the TDAS is largely deformed by the dipole interaction so that H^+ can gain large kinetic energy after the dissociation. Indeed, as shown in Fig. 3.4(d), the kinetic energy of H^+ increases rapidly after $t = 0$. On the other hand, as shown in Fig. 3.4(c), if the ionization timing is -0.7 fs, the O-H distance cannot be stretched so much and is still in the molecular domain of around 1.0 Å at the time when the light field intensity becomes maximum at $t = 0$ fs. Consequently, as shown in Fig. 3.4(f), the increase in the kinetic energy of H^+ becomes slower than in the earlier ionization timings. It can also be seen in Fig. 3.4(g)-(i) that the H-O-H angle becomes larger in the course of the three-body dissociation.

Therefore, it can be said that, when H_2O^{2+} is created in the earlier part of the laser pulse, the duration of the period of the interaction with the intense laser field becomes longer, so that the energy gained from the light field becomes larger in the three-body dissociation.
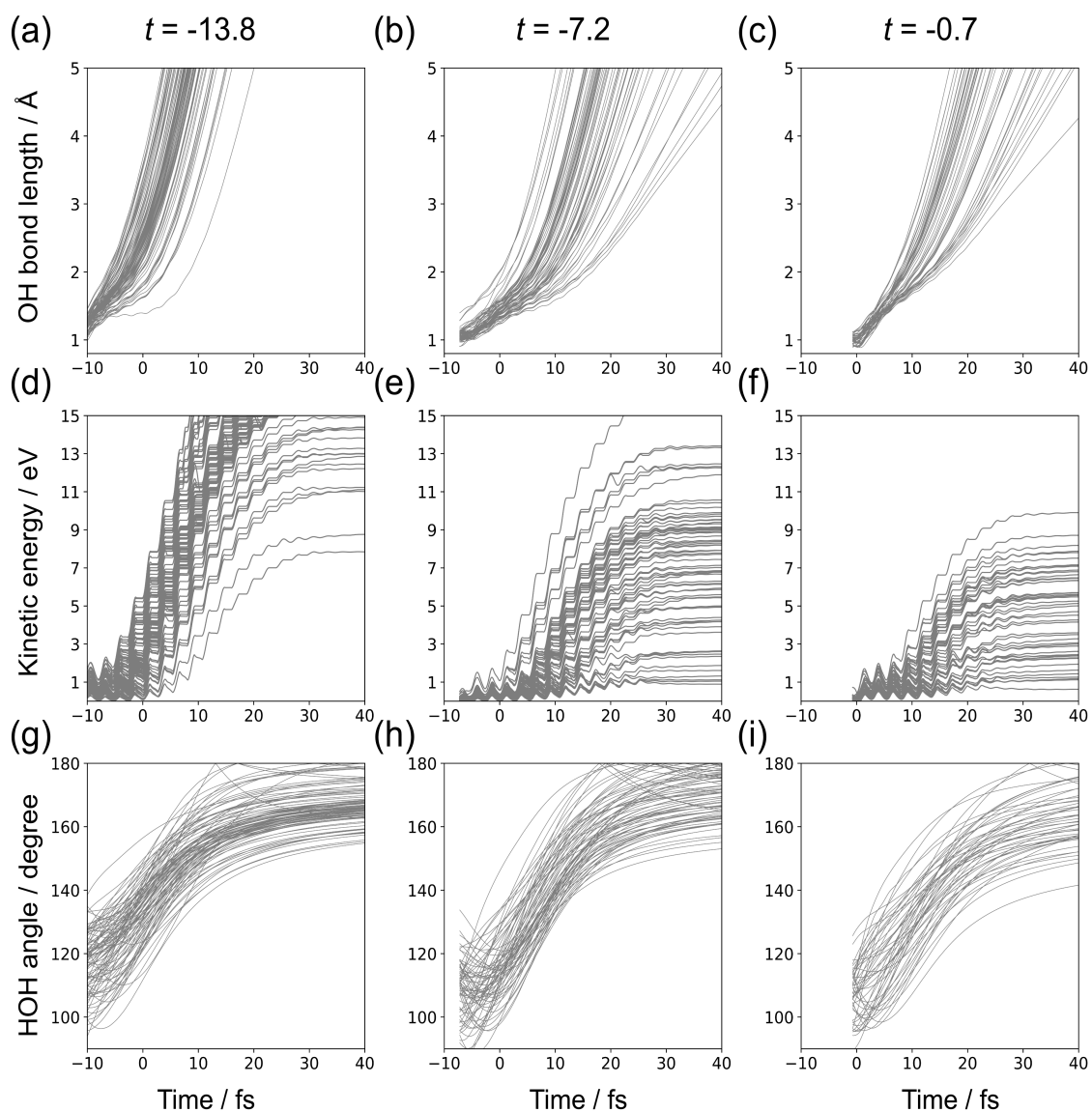
Fig. 3.4. The time evolutions of the length of one of the two O-H bonds, the kinetic energy of one of the two ejected H$^+$s, and the H-O-H bond angle of H$_2$O^{2+} in the course of the three-body dissociation into H$^+$ + O + H$^+$ obtained when H$_2$O^{2+} is created at the ionization timings at -13.8, -7.2, and -0.7 fs in the 20 fs laser pulse. The timings are those with respect to the temporal center of the laser pulse, which is set to be t = 0. It is confirmed that the length of the other O-H bonds and the kinetic energy of the other H$^+$ behave in the same manners as above, respectively.

3.2.2 Ionization probability of H_2O^{2+}

As shown in the preceding section, when H_2O starts interacting with the 8 fs or 20 fs laser pulses, the O-H internuclear distance is kept in the molecular domain in H_2O and H_2O^+ and the stretch of the O-H distance to the large extent is realized only after H_2O^{2+} is created in the three-body decomposition channel. Therefore, considering the experimental finding [11] that the kinetic energy distribution of H^+ ejected through the three-body Coulomb explosion from H_2O^{3+}, $H_2O^{3+} \rightarrow H^+ + O^+ + H^+$, obtained with the 20 fs laser pulse is lowered by as much as 2 eV from that obtained with the 8 fs laser pulse, it is probable that the ionization from H_2O^{2+} to H_2O^{3+} is enhanced at the stretched molecular geometry, which is commonly known as the charge resonance enhanced ionization [14],[15].

In order to clarify the role of the charge resonance enhance ionization, we perform the calculations by the time-dependent configuration interaction method with the complete active space expansion (TD-CASCI) to estimate the ionization probability of H_2O^{2+} in the intense laser field. The time-dependent electronic Schrödinger equation within the dipole approximation at fixed molecular structures is solved in which the eigenenergies and transition dipole moments are calculated at the state-averaged CASSCF [23],[24] level of theory combined with the aug-cc-pVTZ basis set [25] implemented in the Molpro2015 package [26]. The size of the basis set is considered to be sufficiently large to describe the enhanced ionization as was reported by Kraus *et al.* [27] The time propagation is performed by using a split operator technique [28].

We assume that both of the two O-H bonds stretch equally, so that the three-body dissociation,

$$H_2O^{2+} \rightarrow H^+ + O + H^+,$$
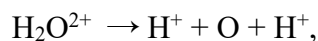
proceeds. In the estimation of the ionization probability, the H-O-H bond angle is also varied as an independent structural parameter. The O-H internuclear distance r is varied from 0.5 Å to 3.0 Å with an equal interval of 0.1 Å and the H-O-H bond angle θ is varied from 100° to 180° with an equal interval of 10°. We calculate the ionization probabilities at the respective mesh points having the different O-H internuclear distance and the H-O-H bond angle.

In order to estimate the extent of the increase in the ionization probability at a given molecular structure, we make H_2O^{2+} interact with the ultrashort near-IR ($\lambda = 800$ nm) light pulse having the pulse width of 3 fs. We assume that the laser pulses have a Gaussian envelope

with a sine-type wave form whose carrier envelope phase is $\pi/2$ and that the maximum laser field intensity is 0.5×10^{15} W/cm^2. We also assume that the laser polarization direction is parallel to the line connecting the two H atoms in H_2O.

We include the lowest 100 electronic states of H_2O^{2+} obtained by the state-averaged CASSCF method in the TD-CASCI calculations. We assume that ionization proceeds from the electronic states whose energies are higher than the ionization threshold $E_{IP}(r, \theta)$, which is defined as the difference between the field-free energy of the electronic ground state of H_2O^{3+}, and that of the electronic ground state of H_2O^{2+} at a given set of the geometrical parameters (r, θ). The numbers of states whose energies are above $E_{IP}(r, \theta)$ at the different molecular structures are in the range of 60-70. We define the ionization probability $P(r, \theta)$ as the sum of the populations in the electronic states whose energies are higher than $E_{IP}(r, \theta)$ at the end of the light pulse because the enhanced ionization rate is considered to be proportional to the depletion in the population of the intermediate resonance states [2],[29].

The results of the calculation plotted in Fig. 3.5(a) shows that the ionization is enhanced especially when 2.5 Å $< r <$ 2.8 Å and 150° $< \theta$ by the charge-resonance enhanced ionization. Figure 3.5(b) shows the trajectories of H_2O^{2+} drawn using the time evolution of the O-H distance (Fig. 3.4(a)) and the H-O-H angle (Fig. 3.4(g)) when the timing of the ionization into H_2O^{2+} is -13.8 fs with the area of the enhanced ionization shown in Fig. 3.5(a). It can be seen in Fig. 3.5(b) that the trajectories evolve and move into the area of the enhanced ionization, which explains well that the ionization to H_2O^{3+} is enhanced in the course of the nuclear motion proceeding on the TDAS of H_2O^{2+}.

By separate calculations, we perform simulations using different laser field intensities in the range of 0.3-1.4 PW/cm^2 and different laser pulse durations at 2 fs and 4 fs. We also perform simulations using a cosine-type wave form. In all these cases of the laser parameters, we confirmed that the O-H distances at which the ionization is enhanced are in the ranges of 2.5 Å $< r <$ 2.8 Å.

The experimental kinetic energies of H^+ reported by Nakano *et al.* [11], 10.8 eV for the 8 fs pulse and 8.9 eV for the 20 fs pulse can be converted respectively to the O-H distances of 1.7 and 2.0 Å just before the three-body Coulomb explosion when θ is assumed to be in the range of 140°-180°. Therefore, it can be said that the trajectories can reach $r = 2.0$ Å on the TDAS of H_2O^{2+} when the pulse duration is 20 fs, so that the ionization to H_2O^{3+} is enhanced

more than in the case of the 8 fs pulse, in which the trajectories cannot go beyond 1.7 Å before the ionization to H_2O^{3+}.

We also perform the TD-CASCI calculations by setting the laser polarization direction to be parallel to the direction of the bisector of the H-O-H angle and by setting it to be perpendicular to the molecular plane, and confirm that, in both of these two cases, the ionization probabilities from H_2O^{2+} to H_2O^{3+} are smaller by six orders of magnitude than in the case treated above, reflecting the fact that the transition dipole responsible for the electronic excitations of H_2O^{2+} is along the b_2 axis as long as H_2O^{2+} keeps C_{2v} molecular symmetry.
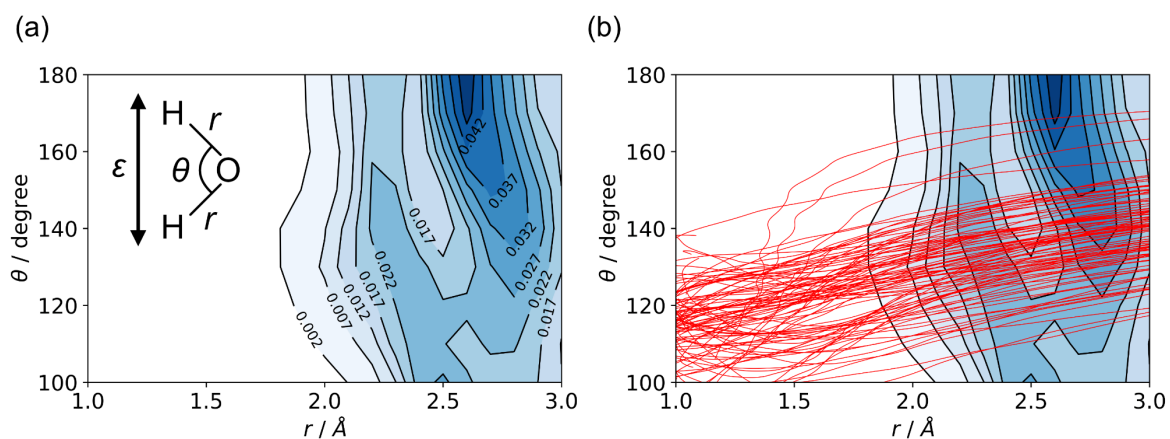

Fig. 3.5. (a) The dependence of the ionization probability of H_2O^{2+} to H_2O^{3+} on the O-H distance and the H-O-H angle calculated by the time-dependent configuration interaction method with the complete active space expansion (TD-CASCI). (b) The trajectories on the TDAS of H_2O^{2+} obtained in Sec. 2.1 when the ionization timing is -13.8 fs with the area of the ionization enhancement shown in (b). The laser polarization direction is represented by ε.

3.3   Summary

We have investigated theoretically the structural deformation and dissociation dynamics of H_2O, H_2O^+, and H_2O^{2+} in a near-IR ($\lambda = 800$ nm) femtosecond intense laser pulse by *ab initio* molecular dynamics calculations combined with the time-dependent adiabatic state approach. We have shown that the peak positions in the kinetic energy distribution of H^+ ejected through the two-body dissociation of H_2O^{2+}; $H_2O^{2+} \rightarrow H^+ + OH^+$, are in good agreement with the experimental data in both 8 fs and 20 fs cases and that, when the double ionization proceeds in the earlier part of the laser pulse, the three-body dissociation of H_2O^{2+}; $H_2O^{2+} \rightarrow$

$H^+ + O + H^+$, dominates, resulting in the broad kinetic energy distribution covering the ranges of 0.5-15 eV (10–54×10^3 u ms^{-1}) for the 8 fs pulse and 0.5-20 eV (10–62×10^3 u ms^{-1}) for the 20 fs pulse.

We have also performed time-dependent configuration interaction calculations to estimate the ionization probability of H_2O^{2+} to H_2O^{3+} and found that the ionization probability is enhanced largely when the two O-H bonds stretch to 2.5-2.8 Å and the H-O-H angle becomes larger than 150° in the linearly polarized light field This finding shows the creation of H_2O^{3+}, leading to the ejection of H^+ via the three-body Coulomb explosion, $H_2O^{3+} \rightarrow H^+ + O^+ + H^+$, proceeds by the charge-resonance enhanced ionization [14],[15] of H_2O^{2+} to H_2O^{3+}.

Acknowledgments

References

[1] H. Kono, S. Koseki, M. Shiota, and Y. Fujimura, *J. Phys. Chem. A* **105**, 5627 (2001).

[2] H. Kono, Y. Sato, N. Tanaka, T. Kato, K. Nakai, S. Koseki, and Y. Fujimura, *Chem. Phys.* **304**, 203 (2004).

[3] K. Yamanouchi, *Science.* **295**, 1659 (2002).

[4] C. Wunderlich, E. Kobler, H. Figger, and T.W. Hänsch, *Phys. Rev. Lett.* **78**, 2333 (1997).

[5] B.M. Garraway and K.-A. Suominen, *Phys. Rev. Lett.* **80**, 932 (1998).

[6] A. Hishikawa, A. Iwamae, and K. Yamanouchi, *Phys. Rev. Lett.* **83**, 1127 (1999).

[7] A. Hishikawa, A. Iwamae, and K. Yamanouchi, *J. Chem. Phys.* **111**, 8871 (1999).

[8] J.H. Sanderson, A. El-Zein, W.A. Bryan, W.R. Newell, A.J. Langley, and P.F. Taday, *Phys. Rev. A* **59**, R2567 (1999).

[9] S. Liu, A. Hishikawa, A. Iwamae, and K. Yamanouchi, in *Adv. Multi-Phot. Process. Spectrosc.* (WORLD SCIENTIFIC, 2000), pp. 189–202.

[10] F. Légaré, K.F. Lee, I. V. Litvinyuk, P.W. Dooley, S.S. Wesolowski, P.R. Bunker, P. Dombi, F. Krausz, A.D. Bandrauk, D.M. Villeneuve, and P.B. Corkum, *Phys. Rev. A* **71**, 013415 (2005).

[11] H. Nakano, Y. Furukawa, A. Ishizawa, K. Hoshina, and K. Yamanouchi, in *2006 Conf. Lasers Electro-Optics 2006 Quantum Electron. Laser Sci. Conf.* (IEEE, 2006), pp. 1–2.

[12] H. Liu, M. Li, X.-G. Xie, C. Wu, Y.-K. Deng, C.-Y. Wu, Q.-H. Gong, and Y.-Q. Liu, *Chinese Phys. Lett.* **32**, 063301 (2015).

[13] Y. Sato, H. Kono, S. Koseki, and Y. Fujimura, *J. Am. Chem. Soc.* **125**, 8019 (2003).

[14] T. Zuo and A.D. Bandrauk, *Phys. Rev. A* **52**, R2511 (1995).

[15] T. Seideman, M.Y. Ivanov, and P.B. Corkum, *Phys. Rev. Lett.* **75**, 2819 (1995).

[16] I. Bocharova, R. Karimi, E.F. Penka, J.-P. Brichta, P. Lassonde, X. Fu, J.-C. Kieffer, A.D. Bandrauk, I. Litvinyuk, J. Sanderson, and F. Légaré, *Phys. Rev. Lett.* **107**, 063201 (2011).

[17] M. Klene, M.A. Robb, M.J. Frisch, and P. Celani, *J. Chem. Phys.* **113**, 5653 (2000).

[18] M.J. Frisch, G.W. Trucks, H.B. Schlegel, G.E. Scuseria, M.A. Robb, J.R. Cheeseman, G. Scalmani, V. Barone, B. Mennucci, G.A. Petersson, H. Nakatsuji, M. Caricato, X. Li, H.P. Hratchian, A.F. Izmaylov, J. Bloino, G. Zheng, J.L. Sonnenberg, M. Hada, M. Ehara, K. Toyota, R. Fukuda, J. Hasegawa, M. Ishida, T. Nakajima, Y. Honda, O. Kitao, H. Nakai, T. Vreven, J.A. Montgomery, Jr., J.E. Peralta, F. Ogliaro, M. Bearpark, J.J. Heyd, E. Brothers, K.N. Kudin,

V.N. Staroverov, R. Kobayashi, J. Normand, K. Raghavachari, A. Rendell, J.C. Burant, S.S. Iyengar, J. Tomasi, M. Cossi, N. Rega, J.M. Millam, M. Klene, J.E. Knox, J.B. Cross, V. Bakken, C. Adamo, J. Jaramillo, R. Gomperts, R.E. Stratmann, O. Yazyev, A.J. Austin, R. Cammi, C. Pomelli, J.W. Ochterski, R.L. Martin, K. Morokuma, V.G. Zakrzewski, G.A. Voth, P. Salvador, J.J. Dannenberg, S. Dapprich, A.D. Daniels, O. Farkas, J.B. Foresman, J. V Ortiz, J. Cioslowski, and D.J. Fox, *Gaussian 09, Revis. A.02, Gaussian, Inc., Wallingford CT* (2009).

[19] V. Veryazov, P.Å. Malmqvist, and B.O. Roos, *Int. J. Quantum Chem.* **111**, 3329 (2011).

[20] M. Barbatti and K. Sen, *Int. J. Quantum Chem.* **116**, 762 (2016).

[21] R. Della Picca, J. Fiol, P.D. Fainstein, J.P. Hansen, and A. Dubois, *J. Phys. B At. Mol. Opt. Phys.* **45**, 194009 (2012).

[22] G.A. McCracken, A. Kaldun, C. Liekhus-Schmaltz, and P.H. Bucksbaum, *J. Chem. Phys.* **147**, 124308 (2017).

[23] P.J. Knowles and H.-J. Werner, *Chem. Phys. Lett.* **115**, 259 (1985).

[24] H. Werner and P.J. Knowles, *J. Chem. Phys.* **82**, 5053 (1985).

[25] T.H. Dunning, *J. Chem. Phys.* **90**, 1007 (1989).

[26] H.-J. Werner, P.J. Knowles, G. Knizia, F.R. Manby, and M. Schütz, *Wiley Interdiscip. Rev. Comput. Mol. Sci.* **2**, 242 (2012).

[27] P. Krause, J.A. Sonk, and H.B. Schlegel, *J. Chem. Phys.* **140**, 174113 (2014).

[28] T. Klamroth, *Phys. Rev. B* **68**, 245421 (2003).

[29] I. Kawata, H. Kono, and Y. Fujimura, *J. Chem. Phys.* **110**, 11152 (1999).

Chapter 4.

Extension of heuristic model to estimate ionization rate

This chapter is not published because it is scheduled to be published in journals or other publications within five years.

Chapter 5.

Summary and future perspectives

In this thesis, I performed theoretical calculations to investigate the molecules in intense laser fields.

In Chapter 3, I performed theoretical calculations and established the assignment of the observed peak profiles to interpret the experimental findings. In the previous study [1], it was found that the momentum distribution of protons ejected from H_2O in an ultrashort intense laser field exhibited multiple peak profiles and that these profiles vary sensitively to the laser pulse. First, I performed *ab initio* molecular dynamics calculations combined with the time-dependent adiabatic state approach [2] to examine the effect of the laser field on the momentum distribution of protons ejected from H_2O^{2+}. I also performed time-dependent configuration interaction calculations with complete active space expansion to examine the ionization process of H_2O^{2+}.

I showed that the peak positions of the momentum distribution of H^+ ejected through the two-body dissociation of H_2O^{2+} are in good agreement with the experimental data. I also revealed that the charge resonance enhanced ionization of H_2O^{2+} plays an import role in the formation of H_2O^{3+}.

In Chapter 4, I developed the extension of heuristic model proposed by Klinkusch *et al.* [3] in which the ionization process is treated using complex energies in energy space in the time-dependent configuration interaction singles method. The complex energies are calculated from the orbital energies with an arbitrary length parameter d. This heuristic model was extended to be implementable in the general class of time-dependent configuration interaction methods.

I demonstrated the original heuristic model and the extended heuristic model to calculate resonance enhanced ionization rates of H_2^+ and H_2. The results basically reproduced the curves of the ionization rates as a function of internuclear distance calculated in the previous study using grid-based time-dependent Schrödinger equation [4] and full-dimensional time-dependent Schrödinger equation [5].

I expect that this extended heuristic model can be combined with *ab initio* molecular dynamics using the time-dependent adiabatic state approach so that we can describe the molecular dynamics with the ionization process in intense laser fields. By calculating semi-classical electronic time-dependent Schrödinger equation in the time-dependent adiabatic state

picture simultaneously with the nuclear moving at each time step, the ionization probability is expected to be estimated for simulating the ionization process in *ab initio* molecular dynamics calculation. This may help us to understand phenomena of molecules in intense fields.

Reference

[1] H. Nakano, Y. Furukawa, A. Ishizawa, K. Hoshina, and K. Yamanouchi, in *2006 Conf. Lasers Electro-Optics 2006 Quantum Electron. Laser Sci. Conf.* (IEEE, 2006), pp. 1–2.

[2] Y. Sato, H. Kono, S. Koseki, and Y. Fujimura, *J. Am. Chem. Soc.* **125**, 8019 (2003).

[3] S. Klinkusch, P. Saalfrank, and T. Klamroth, *J. Chem. Phys.* **131**, 114304 (2009).

[4] A. Bandrauk and F. Légaré, *Progress in Ultrafast Intense Laser Science VIII* (Springer Berlin Heidelberg, Berlin, Heidelberg, 2012).

[5] E. Dehghanian, A.D. Bandrauk, and G.L. Kamta, *Phys. Rev. A* **81**, 061403 (2010).

Acknowledgements

I was supported by many people in my Ph.D. course. I wish to show my feeling of gratitude to those who helped me.

First of all, I would like to thank my supervisor Prof. Kaoru Yamanouchi for giving me a wonderful environment to do research. Moreover, I am very grateful to Prof. Kaoru Yamanouchi for taking the time for discussions and giving me a lot of significant advice and encouragements.

I would like to express my deep gratitude to Prof. Hirohiko Kono for giving me guidance about how to design the theoretical calculations and how to tackle the problems. I learned not only a lot of knowledge and skills but also the way of thinking for doing research.

I would like to show my appreciation to Dr. Kaoru Yamazaki for teaching me a lot of practical useful techniques and knowledge. Much information from Dr. Kaoru Yamazaki helps me to conduct my research.

I would also like to thank all the members in quantum chemistry laboratory for letting me have a very enjoyable time. They gave me a lot of interesting ideas and advice in the group seminars and discussions.

I appreciate the computational resource support from Research Center for Computational Science, Okazaki, Japan.

At last, I owe a debt of gratitude to my parents for their warm support over my Ph.D. course.